

PIONIC 2p-1s TRANSITIONS IN ^{16,18}O

by

PAUL ARTHUR ROUTENBURG

B.Sc., University of Waterloo, 1983

A THESIS SUBMITTED IN PARTIAL FULFILLMENT

OF THE REQUIREMENTS FOR THE DEGREE OF

MASTER OF SCIENCE

in the Department of


Physics


We accept this thesis as conforming


to the required standard


G.A. Beer


G.R. Mason


A. Olin


W.J. Balfour


P.R. West

© PAUL ARTHUR ROUTENBURG

University of Victoria

August 1985

All rights reserved. This thesis may not be reproduced
in whole or in part, by mimeograph or other means
without the permission of the author.

ACCEPTED

FACULTY OF GRADUATE STUDIES

DEAN

Oct 31, 85

QC793.5
M425R68

ACCEPTED
SOCIETY OF GRADUATE STUDENTS

Supervisor: Dr George A. Beer

ABSTRACT

In an attempt to resolve the discrepancy between previous measurements of the pionic 2p-1s transition in the isotope pair $^{16,18}\text{O}$ another measurement has been made using a recently-developed Compton suppression spectrometer. The resulting reduction of the Compton background has allowed a more confident determination of the energies, shifts and Lorentzian widths of the 2p-1s transitions. The results obtained were:

	E (keV)	ϵ (keV)	Γ (keV)
^{16}O	160.388(.083)	-15.02(.09)	6.94(.31)
^{18}O	156.044(.119)	-19.38(.13)	6.71(.39)

The resultant Isotope Effect is:

$$\Delta\epsilon_{1s} = \epsilon_{1s} (^{18}\text{O}) - \epsilon_{1s} (^{16}\text{O}) = -4.36(.16) \text{ keV}$$

$$\Delta\Gamma_{1s} = \Gamma_{1s} (^{18}\text{O}) - \Gamma_{1s} (^{16}\text{O}) = -0.23(.50) \text{ keV}$$

Examiners:

G.A. Beer

G.R. Mason

A. Olin

W.J. Balfour

P.R. West

TABLE OF CONTENTS

ABSTRACT	ii
TABLE OF CONTENTS	iii
LIST OF TABLES	v
LIST OF FIGURES	vii
ACKNOWLEDGEMENTS	ix
DEDICATION	x

<u>Chapter</u>	<u>Page</u>
1. INTRODUCTION	1
2. THEORETICAL APPROACH TO PIONIC ATOMS	
Introduction	7
Pion-Nucleon Scattering	9
The π -Nucleus Optical Potential	13
Nuclear Medium Effects	17
Pion Absorption	20
Isotope Effects in Pionic Atoms	23
3. THE EXPERIMENTAL METHOD	
Introduction	26
Experimental Arrangement	29
The X ray Detection System	34

	The Data Acquisition System and Electronics	38
	Scintillator Telescope Logic	40
	Germanium Detector Logic	42
	BGO Logic	43
	Trigger Logic	45
4.	DATA ANALYSIS	
	Introduction	46
	The Peak Fitting Program	47
	The Detector Response Function	50
	Energy Calibration	58
	Analysis of the π^{160} 2p-1s X-ray Line	62
	Analysis of the π^{180} 2p-1s X-ray Line	67
5.	DISCUSSION OF RESULTS AND CONCLUSIONS	
	Theoretical Predictions	75
	Comparison of Results With Theory and Other Experiments	78
	Conclusions	87
	REFERENCES	88

LIST OF TABLES

<u>Table</u>	<u>Page</u>
1. Peaks Used to Determine Detector Efficiency	56
2. Tailing Data.	57
3. Energy Calibration Peaks (Set I).	58
4. Energy Calibration Peaks (Set II)	59
5. Energy Calibration Peaks (Set III).	59
6. Peaks in the π^{160} 2p-1s Fitting Window	66
7. Peaks in the π^{180} 2p-1s Fitting Window (Set I)	69
8. Peaks in the π^{180} 2p-1s Fitting Window (Set II).	70
9. Final Results	74
10. Contributions to the Uncertainties in the Energies and Widths of the $\pi^{16,180}$ 2p-1s X rays.	74
11. Optical Potential Parameters.	76
12. Charge and Matter Distributions Used in the Theoretical Calculations of Energies and Linewidths.	77
13. Comparison of the Measured Energies, Shifts and Widths of the $\pi^{16,180}$ X rays With Other Experiments and Theory.	79

<u>Table</u>	<u>Page</u>
14. Comparison of Experimental Energies (in keV) of the $\mu^{16,180}$ np-1s X rays.	84
15. Isotope Effects Compared to Other Experiments and Theory	86

LIST OF FIGURES

<u>Figure</u>	<u>Page</u>
1. Effects of the Strong Interaction.	4
2. Arrangement of the M13 Channel	27
3. Experimental Arrangement	30
4. Time-of-Flight Spectrum	33
5. BGO Compton Suppressor	35
6. The Complete Electronics	39
7. Scintillator Telescope Logic	41
8. Ge Detector Logic	41
9. BGO Logic	44
10. Trigger Logic	44
11. Resolution as a Function of Energy	51
12. Ba/Co Source Spectrum	53
13. Relative Efficiency from Barium and Cobalt Sources	55
14. Energy Calibration	61
15. π^{160} Regions and Peaks	64
16. π^{160} Final Fit	65
17. π^{180} Regions and Peaks	68
18. π^{180} Final Fit (Set I)	72
19. π^{180} Final Fit (Set II)	73

<u>Figure</u>	<u>Page</u>
20. Comparison of Experimental π^{160} 2p-1s Energies, Shifts and Widths.	80
21. Comparison of Experimental π^{180} 2p-1s Energies, Shifts and Widths.	81

ACKNOWLEDGEMENTS

I would like to thank those who donated their time and skill to make this experiment a success: G. Beer, D. Britton, R. Kunselman, J. MacDonald, G. Mason, T. Numao, A. Olin and B.H. Olaniyi. I would also like to thank A. Olin whose advice on various aspects of the experiment proved most valuable. My final thanks go to my supervisor G.A. Beer for his encouragement and assistance throughout this project.

To Elisabet . . .

CHAPTER 1

INTRODUCTION

The pion (pi-meson) was first proposed in 1935 (Yukawa) as the strong interaction analogue to the photon. This followed from the well established theory that charged particles interacted by an exchange of photons. Shortly after the discovery of the pion (Lattes et al., 1947), both Fermi and Teller (1947) and Wheeler (1947) predicted the existence of mesic atoms. The first conclusive evidence for the existence of pionic atoms was obtained (Camac et al., 1952) for negative pions stopping in carbon.

A negative pion passing through matter is slowed down by electromagnetic interactions with nearby atoms. It will then be slowed down further by collisions with electrons of comparable velocities until finally it is captured by an atom into a high atomic orbit, forming a pionic atom. The particle then cascades down to lower orbits, first by Auger electron processes and later by radiative transitions involving the emission of X rays. Finally, the particle in a state of low angular momentum will be captured by the nucleus through the strong interaction.

The radius of the Bohr orbit with principal quantum number n is given by

$$r_n = \frac{\hbar^2 n^2}{\mu e^2 Z} \quad (1)$$

where μ is the reduced mass of the pion and Ze the nuclear charge. If it is assumed that the pion begins its cascade just inside the innermost electron orbit, we find from (1) that

$$n_\pi = (m_\pi/m_e)^{1/2} \approx 16 \quad (2)$$

Since the pion spends most of its time within the electron cloud, electron screening effects are negligible for most applications. Thus, the pionic atom can be treated as a hydrogen-like atom and the higher energy levels can be calculated from electromagnetic theory.

As the pion cascade reaches values of lower n the overlap between the pion and nuclear wavefunctions increases and the strong interaction begins to play an important role. At some final n -value nuclear absorption will dominate, the pion will be captured and the X-ray series will terminate. In general the pion will feel the effects of the strong interaction only in the lowest level before nuclear absorption occurs. This is due to the short range nature of the strong interaction which changes by several orders of magnitude for each step in orbital quantum number n .

The strong interaction between the pion and the nucleus causes a shift in the energy of the last observable X-ray

transition from the purely electromagnetic value. In addition, because nuclear absorption reduces the lifetime of the final atomic state, the time-energy uncertainty principle dictates that the pion's energy be spread out over a finite width. Thus, what is observed in an X-ray spectrum is a broadened X-ray whose energy is shifted from that expected from a purely electromagnetic transition (see Figure 1). Precise measurements of the X-ray energy spectrum then allow the energy shift (ϵ) and width (Γ) associated with the final atomic state to be determined.

The most common theoretical approach to describing pionic atoms makes use of a macroscopic approach. In this approach a purely phenomenological optical model is used in which the parameters of the potential representing the interaction between the pion and the nucleus are adjusted to give a good fit to the experimental data. The optical model has had considerable success in fitting strong interaction measurements of pionic atoms during the last decade.

The strong interaction between the orbiting pion and the nucleus is described by a pion-nuclear potential derived by Ericson and Ericson (1966) who use a multiple scattering approach. The nucleus is treated as a collection of fixed scatterers, with the bound pion considered to scatter off the individual nucleons at zero energy. This scattering is

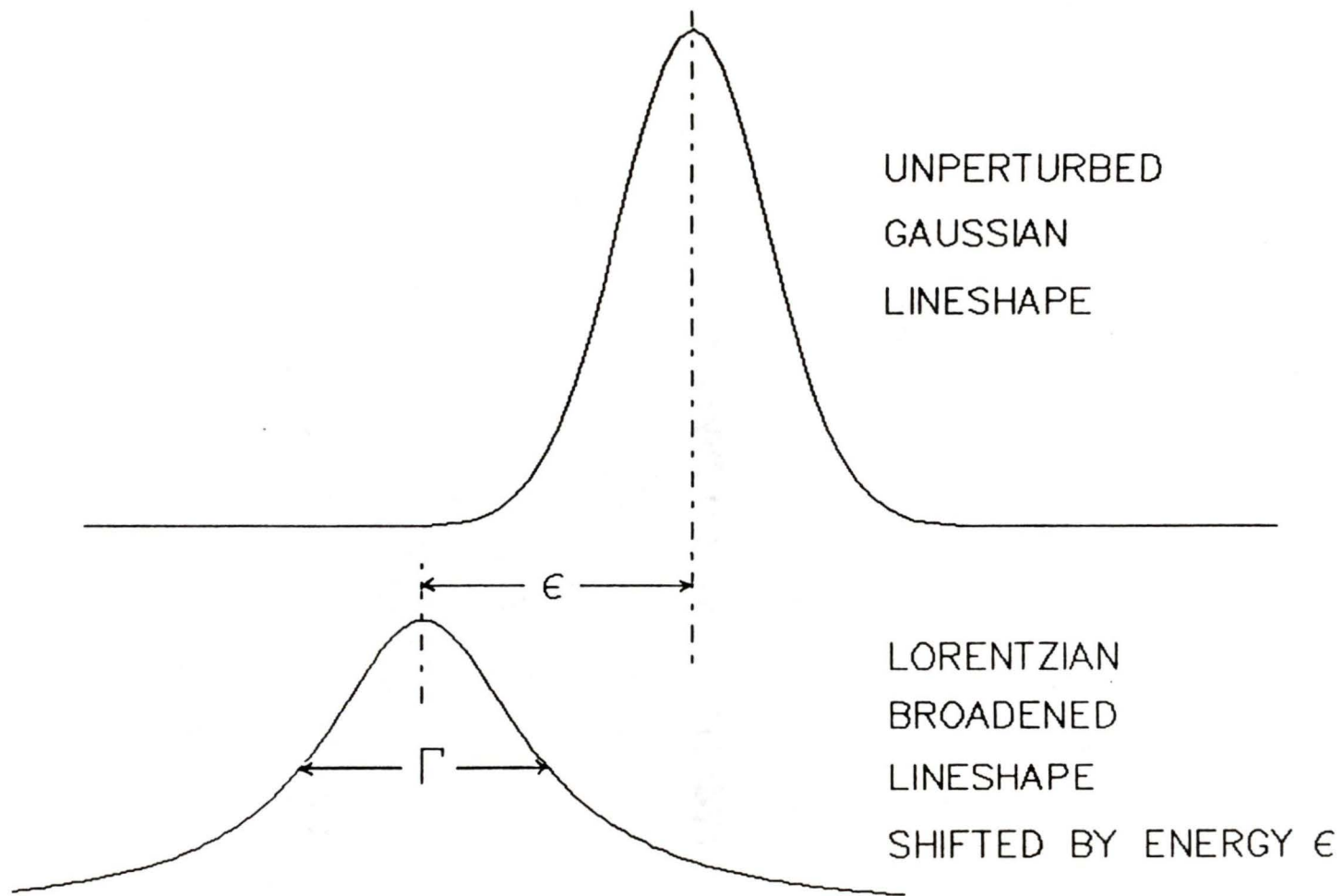


Figure 1: Effects of the Strong Interaction

averaged over the continuous nuclear matter distribution with the granularity in the nuclear structure taken into account mainly through the Lorentz-Lorenz effect.

The aim of this thesis project was to obtain a new measurement of the strong interaction shift and width of the pionic 2p-1s transition in the isotopes 16,180 . Previous measurements of the isotope effects of 16,180 are in disagreement, and by repeating the measurement with an effective background suppression it was hoped that this disagreement would be resolved. Background suppression was achieved with a Compton suppressor system that reduced the background due to Compton scattered photons.

The first measurements on the 16,180 isotope pair were made in 1967 and have been repeated several times since. The isotope 180 is particularly interesting since it is one of two isospin 1 nuclei with Z low enough that the 2p-1s transition is observable (the other being ^{22}Ne). An accurate measurement of the isotope shifts

$$\Delta\varepsilon_{1s} = \varepsilon_{1s} (^{180}) - \varepsilon_{1s} (^{160}) \quad (3)$$

$$\Delta\Gamma_{1s} = \Gamma_{1s} (^{180}) - \Gamma_{1s} (^{160})$$

reflects the effect of adding two neutrons to the doubly magic nucleus ^{16}O . Results lead to a more stringent determination of the isovector terms in the optical model.

The theoretical description of pionic atoms within the framework of the optical model is outlined in Chapter 2. In Chapter 3 details of the experiment are presented, while Chapter 4 is devoted to a discussion of the analysis of the data obtained in this experiment. Finally, in Chapter 5 the results are presented and compared with previous experimental results and optical model predictions.

CHAPTER 2

THEORETICAL APPROACH TO PIONIC ATOMSIntroduction

The pionic atom is a system consisting of a pion and an atomic nucleus. The atomic levels between which the observed X-ray transitions occur are essentially the same as the levels of a normal electronic hydrogen atom. Thus, the simple Bohr formulas lead to a good understanding of these energy levels:

$$E_n = - \frac{\mu c^2 (Z\alpha)^2}{2 n^2} \tag{4}$$
$$r_n = \frac{\hbar^2 n^2}{\mu e^2 Z}$$

where E_n is the energy of the level with principal quantum number n and r_n is the radius of the corresponding Bohr orbit; α is the fine structure constant and μ the reduced mass of the orbiting pion.

The motion of the orbiting pion about the nucleus is described more accurately by the relativistic Klein-Gordon equation (since pions are bosons with spin 0)

$$\left\{ \hbar^2 \nabla^2 + \frac{1}{c^2} [(E - V_e)^2 - \mu^2 c^2] \right\} \psi = 2\mu V_N \psi. \quad (5)$$

Two potential terms are included: V_e is the electromagnetic potential due to the distributed nuclear charge $+Ze$ and V_N is the strong interaction potential due to all of the nucleons in the nucleus. The potential V_e contains the effects of the finite extent of the nuclear charge and the first order vacuum polarization. Higher orders of vacuum polarization and electron screening effects are negligible for the lower transitions in pionic atoms. The potential V_N is usually derived using an optical model, in which the strong pion-nucleus interaction is treated in analogy with the scattering of light by a homogeneous optical medium with a complex index of refraction (Lax, 1952).

The optical potential which is used to describe low energy pion-nucleus scattering and which incorporates the pion-nucleon scattering amplitudes is described in the following sections. Modifications are included to allow for the difference between pion-nucleon (π -N) scattering in free space and π -N scattering inside nuclear matter. An imaginary term is also added to the optical potential to account for pion absorption.

Pion-Nucleon Scattering

Since the pion is in a well defined state of angular momentum, λ , with respect to the nucleus, the interaction of the pion with the nucleus can be considered as a sum of pion-nucleon elastic scatterings. Considering for the moment only spin and angular momentum states and an incoming plane wave $\psi = e^{ikz}$, we have for the outgoing wave

$$\psi_{\text{out}} = e^{ikz} + f(E, \theta) \frac{e^{ikr}}{r} \quad (6)$$

where e^{ikz} is the undisturbed part of the incoming wave and e^{ikr}/r is the scattered wave having amplitude $f(E, \theta)$. The dependence of the scattering amplitude on the energy of the incoming particle is explicitly included.

For spinless particles (eg., a pion), the scattering amplitude can be expanded in terms of the Legendre polynomials $P_\lambda(\cos\theta)$ in a partial-wave expansion:

$$f(E, \theta) = \sum_{\lambda=0}^{\infty} (2\lambda+1) f_\lambda P_\lambda(\cos\theta). \quad (7)$$

However, as the partial wave amplitudes f_λ depend on the spin of the nucleon, Equation (7) must be modified. In the case of pionic atoms, low energies and momenta are involved; thus,

the expansion (7) can be restricted to include only the s and p partial waves. It can be shown (Williams, 1971) that $f(E, \theta)$ can be written:

$$f(E, \theta) \approx f_{s_{1/2}} + (f_{p_{1/2}} + 2f_{p_{3/2}}) \cos \theta - \frac{i \underline{\sigma} \cdot \underline{k} \times \underline{k}'}{|\underline{k} \times \underline{k}'|} (f_{p_{1/2}} - f_{p_{3/2}}) \sin \theta \quad (8)$$

where \underline{k} and \underline{k}' are the incoming and outgoing pion momenta and $\underline{\sigma}$ is the Pauli spin operator (' \underline{k} ' indicates that ' k ' is a vector).

The π -N scattering lengths may be defined as

$$a_{\lambda j} = \lim_{k \rightarrow 0} \frac{f_{\lambda j}}{k^{2\lambda}} \quad (9)$$

Since the bound pion can be considered to scatter off the nucleus at zero incident energy, the partial wave amplitudes $f_{\lambda j}$ can be written in terms of the scattering lengths, i.e.,

$$f_{\lambda j} = a_{\lambda j} k^{2\lambda} \quad (10)$$

E is a constant, and so $f(E, \theta)$ becomes

$$f(\theta) = a_{s_{1/2}} + (a_{p_{1/2}} + 2a_{p_{3/2}}) k^2 \cos\theta - \frac{i\sigma \cdot \underline{k} \underline{k}'}{|\underline{k} \underline{k}'|} (a_{p_{1/2}} - a_{p_{3/2}}) k^2 \sin\theta. \quad (11)$$

If the nucleon scatterers are considered fixed and the scattering is elastic, $|\underline{k}| = |\underline{k}'|$, and

$$\begin{aligned} k^2 \cos\theta &= \underline{k} \cdot \underline{k}' \\ k^2 \sin\theta &= |\underline{k} \times \underline{k}'| \end{aligned} \quad (12)$$

With these substitutions Equation (11) becomes

$$f(\theta) = a_{s_{1/2}} + (a_{p_{1/2}} + 2a_{p_{3/2}}) \underline{k} \cdot \underline{k}' - i\sigma \cdot \underline{k} \times \underline{k}' (a_{p_{1/2}} - a_{p_{3/2}}). \quad (13)$$

The final task is to decompose the scattering amplitudes of Equation (13) into different isospin components. We begin by defining the isospin projection operators

$$Q_- = 1/3 (1 - \underline{t} \cdot \underline{\tau}), \quad Q_+ = 1/3 (2 + \underline{t} \cdot \underline{\tau}), \quad (14)$$

for the total isospin states $T=1/2$ and $T=3/2$, respectively, that are available to the π -N system. \underline{t} and $\underline{\tau}$ are, respectively, the pion and nucleon isospin.

The scattering lengths may now be decomposed as

$$\begin{aligned} a &= \sum_T Q_T a(T) = 1/3 (1-\underline{t}\cdot\underline{\tau})a(1/2) + 1/3 (2+\underline{t}\cdot\underline{\tau})a(3/2) \\ &= 1/3 (a(1/2) + 2a(3/2)) + 1/3 (a(3/2) - a(1/2))\underline{t}\cdot\underline{\tau} \end{aligned} \quad (15)$$

where T is the total isospin. If we define the s-wave scattering length as a_{2T} and the p-wave scattering volume as a_{2T2J} the scattering lengths of Equation (13) may be written as:

$$\begin{aligned} a_{s_{1/2}} &= 1/3 (a_1 + 2a_3) + 1/3 (a_3 - a_1)\underline{t}\cdot\underline{\tau} \\ a_{p_{1/2}} &= 1/3 (a_{11} + 2a_{31}) + 1/3 (a_{31} - a_{11})\underline{t}\cdot\underline{\tau} \\ a_{p_{3/2}} &= 1/3 (a_{13} + 2a_{33}) + 1/3 (a_{33} - a_{13})\underline{t}\cdot\underline{\tau} \end{aligned} \quad (16)$$

Making these substitutions, Equation (13) becomes

$$f(\theta) = b_0 + b_1 \underline{t}\cdot\underline{\tau} + [c_0 + c_1 \underline{t}\cdot\underline{\tau}] \underline{k}\cdot\underline{k}' - i[d_0 + d_1 \underline{t}\cdot\underline{\tau}] \underline{\sigma}\cdot\underline{k}\underline{k}' \quad (17)$$

where

$b_0 = 1/3 (2a_3 + a_1)$, the isoscalar s-wave parameter

$b_1 = 1/3 (a_3 - a_1)$, the isovector s-wave parameter

$c_0 = 1/3 (2a_{31} + 4a_{33} + a_{11} + 2a_{13})$, the isoscalar p-wave parameter

$c_1 = 1/3 (a_{31} + 2a_{33} - a_{11} - 2a_{13})$, the isovector p-wave parameter

$d_0 = 1/3 (2a_{31} - 2a_{33} + a_{11} - a_{13})$, the isoscalar spin-dependent s-wave parameter

$d_1 = 1/3 (a_{31} - a_{33} - a_{11} + a_{13})$, the isovector spin-dependent p-wave parameter

The magnitudes of the spin dependent terms d_0 and d_1 have been estimated by, for example, Friedman (1980), and they can be neglected in this work.

The π -Nucleus Optical Potential

The most common approach used to describe the effects of the strong interaction is through the use of the so-called Optical potential, based on the elementary processes



The pi-nucleus interaction can be described in terms of the potential

$$V_{\text{opt}} = \text{Re}(V) + i\text{Im}(V). \quad (18)$$

The imaginary term in (18) arises from pion absorption which will be discussed in a subsequent section.

The nucleus is a many-body system composed of protons and neutrons. The free π -N scattering amplitude derived in the previous section may be written for the i 'th nucleon in the nucleus as (neglecting spin dependent terms)

$$f_i(\theta) = \{b_0 + b_1 \underline{t} \cdot \underline{\tau} + [c_0 + c_1 \underline{t} \cdot \underline{\tau}] \underline{k} \cdot \underline{k}'\} \delta(\underline{r} - \underline{r}') \quad (19)$$

where it is assumed that the scattering amplitude of pions from free and bound nucleons is the same, apart from kinematical factors. This 'impulse approximation' is expected to be good for the low pion energies that are relevant here (Ericson and Ericson, 1966).

To obtain the total scattering amplitude, the component for the i 'th nucleon must be summed over all the nucleons in the nucleus. This is done under the frozen nucleus approximation where the positions of the nucleons are assumed to be undisturbed by the scattering pion, that is, nuclear recoil effects are ignored.

Ignoring nuclear absorption, the interaction of the bound pion with the nucleus can be regarded as a kind of low energy elastic scattering (Ericson, 1970). If one introduces a short range pseudopotential $V(\underline{r})$, for which the scattering amplitude is given by

$$f(\theta) = - \frac{m_{\pi}}{2\pi\hbar^2} \int e^{-i\underline{k}\cdot\underline{r}} V(\underline{r}) e^{i\underline{k}'\cdot\underline{r}} d\underline{r} \quad (20)$$

then $V(\underline{r})$ can be found from the inversion of this pseudopotential:

$$V(\underline{r}) = - \frac{2\pi\hbar^2}{m_{\pi}} \int f(\theta) e^{-i(\underline{k}-\underline{k}')\cdot\underline{r}} d^3(\underline{k}-\underline{k}'). \quad (21)$$

With the identity

$$\underline{k} = -i(\underline{\nabla} e^{i\underline{k}\cdot\underline{r}}) e^{-i\underline{k}\cdot\underline{r}},$$

terms of the form $\underline{k}\cdot\underline{k}'\rho(r)$ are transformed to terms of the form $\underline{\nabla}\rho(\underline{r})\underline{\nabla}$, and the nuclear potential $V(\underline{r})$ is obtained (Backenstoss, 1970).

$$\begin{aligned}
 V_N(\underline{r}) = & - \frac{2\pi\hbar^2}{\mu_\pi} \{b_0\rho(\underline{r}) + b_1[\rho_n(\underline{r}) - \rho_p(\underline{r})] \\
 & + \frac{\nabla}{f} (c_0\rho(\underline{r}) + c_1[\rho_n(\underline{r}) - \rho_p(\underline{r})])\nabla\}
 \end{aligned}
 \tag{22}$$

where $\rho(\underline{r}) = \rho_n(\underline{r}) + \rho_p(\underline{r})$ is the sum of the neutron density $\rho_n(\underline{r})$ and the proton density $\rho_p(\underline{r})$, and μ_π is the reduced mass of the π -nucleus system. It quickly became apparent, however, that when theoretical and experimental level shifts were compared, this first approximation (Equation (22) with $\xi = 0$ (see page 19)) was inadequate.

The potential (22) must be modified to include nucleon-nucleon correlations and pion absorption. The short range nucleon-nucleon correlations give rise to the Lorentz-Lorenz effect in the p-wave interaction, exhibited by the factor f in the above equation. This effect is discussed in the next section.

Nuclear Medium Effects

The assumption of a homogeneous nucleus that has been implicit so far must be replaced with a description that includes nucleon-nucleon correlations. This granular property of nuclear matter gives rise to two effects, a repulsive s-wave interaction and the Lorentz-Lorenz effect in the p-wave interaction.

The repulsive nature of the s-wave interaction is discussed first. In a first approximation, if the nucleus is homogeneous, s-wave scattering off the nucleus can be considered as the sum of scattering off the individual nucleons with a potential (Backenstoss, 1970)

$$V_N(\underline{r}) = - \frac{2\pi\hbar^2}{\mu_\pi} \left[\frac{Z}{A} a_{\pi-p} + \frac{A-Z}{A} a_{\pi-n} \right] \rho(\underline{r}). \quad (23)$$

However, the term $a_{\pi-p} = b_0 - b_1$ is almost equal to, but opposite in sign from, the term $a_{\pi-n} = b_0 + b_1$, so that the two terms in V_N almost cancel. The remaining interaction does not sufficiently account for the observed 1s level shifts. The assumption of a homogeneous and uniform nucleus with no discrete structure must therefore be replaced.

The normal nucleon field seen by the incident wave is replaced with an effective field due to the correlations of pairs of nucleons. The pion inside the nucleus views the nearby nucleon as concentrated at a point, surrounded by a hole in the nuclear medium. The effective field within the hole is given by the overall average field ϕ_{ave} , modified by the removal of uniform matter within the hole (Ericson, 1970)

$$\begin{aligned}\phi_{\text{eff}} &= \frac{1}{1 + a\left(\frac{1}{r}\right)_{\text{hole}}} \phi_{\text{ave}} \\ &= \phi_{\text{ave}} \left[1 - a\left(\frac{1}{r}\right)_{\text{hole}} + \dots \right]\end{aligned}\tag{24}$$

where a is the π -N s-wave scattering length, and $\left(\frac{1}{r}\right)_{\text{hole}}$ is the expectation value of the inverse correlation length. a is then replaced by an effective s-wave scattering length

$$a_{\text{eff}} \approx a - a^2\left(\frac{1}{r}\right)_{\text{hole}}\tag{25}$$

The linear term in a is small and so the main contribution is from the a^2 term, which makes a_{eff} negative, leading to the observed repulsive nature of the s-wave

interaction. The main contribution to this effect is from Pauli correlations, which give the largest values of $(\frac{1}{r})_{\text{hole}}$. This effect is known as Pauli blocking.

The second effect of nucleon-nucleon correlations is an important modification of the p-wave term in the optical potential known as the Lorentz-Lorenz effect. This effect is similar to the change of the dielectric constant in a material due to atom-atom correlations being taken into account. The dipole component in π -N scattering produces a nuclear Lorentz-Lorenz effect when nucleon-nucleon correlations are considered.

This effect is exhibited by the factor f

$$f = 1 + \xi \frac{4\pi}{3} \{c_0 \rho(\underline{r}) + c_1 [\rho_n(\underline{r}) - \rho_p(\underline{r})]\} \quad (26)$$

which modifies the p-wave term in Equation (22) to

$$\frac{\nabla}{1 + \xi \frac{4\pi}{3} \{c_0 \rho(\underline{r}) + c_1 [\rho_n(\underline{r}) - \rho_p(\underline{r})]\}} \frac{\nabla}{\{c_0 \rho(\underline{r}) + c_1 [\rho_n(\underline{r}) - \rho_p(\underline{r})]\}} \quad (27)$$

where ξ is the Lorentz-Lorenz parameter describing the strength of the effect; $\xi = 0$ reproduces the original p-wave

term and $\xi = 1$ corresponds to short-range nucleon-nucleon correlations.

In calculations by Powers et al. (1980), ξ was allowed to float freely in fits to pionic atom data and values of $\xi > 1$ were found. However, the values of ξ obtained depended very strongly on the values used for the neutron radii. Since $\rho_n(r)$ and ξ could not be determined simultaneously, further independent information about either one is required before the question of the value of ξ is resolved.

Pion Absorption

If the nuclear potential V_N is to describe the process of pion absorption mentioned previously, an imaginary part must be added to it. The absorption process



is characterised by the fact that in nuclear matter it must occur on a pair of nucleons.

The pion in a bound state essentially has zero momentum, whereas the pion mass liberated in the absorption process amounts to 140 MeV. Conservation of energy and momentum demands that the nucleon which absorbs a pion needs a Fermi momentum of about 500 MeV/c. Since the Fermi momentum in

nuclei is typically lower, absorption on a single nucleon is unlikely. However, if the pion is absorbed at a correlated nucleon pair as suggested by Brueckner et al. (1951), the final state can easily have zero momentum when the two nucleons share the liberated energy and leave with opposite momentum.

In order to include pion absorption in the potential V_N an imaginary part is added to both the local (s-wave) and non-local (p-wave) terms of the potential. A final trivial modification must be made to the potential due to kinematical considerations since a bound nucleon does not recoil as a free nucleon does. The free scattering amplitude of Equation (17) must be modified by the factor $p_1 = (1 + \mu/m)$ for zero energy interactions, where μ and m denote the pion and nucleon mass respectively. Similarly, the potential terms quadratic in density are modified by the factor $p_2 = (1 + \mu/2m)$ where the factor of 2 is due to the two nucleon nature of pion absorption as discussed above.

The complete nuclear potential used to describe the pion-nucleus system becomes

$$\begin{aligned}
 V_N(\underline{r}) = & - \frac{2\pi\hbar^2}{2\mu_\pi} \{ p_1 b_0 \rho(\underline{r}) + p_1 b_1 [\rho_n(\underline{r}) - \rho_p(\underline{r})] + p_2 B_0 \rho^2(\underline{r}) \\
 & + \underline{\nabla} \frac{1}{f} (p_1 c_0 \rho(\underline{r}) + p_1 c_1 [\rho_n(\underline{r}) - \rho_p(\underline{r})] + p_2 C_0 \rho^2(\underline{r})) \underline{\nabla} \}
 \end{aligned}
 \tag{28}$$

with

$$f = 1 + \xi \frac{4\pi}{3} \{p_1 c_0 \rho(\underline{r}) + p_1 c_1 [\rho_n(\underline{r}) - \rho_p(\underline{r})] + p_2 c_0 \rho^2(\underline{r})\}.$$

The terms $B_0 \rho^2(\underline{r})$ and $C_0 \rho^2(\underline{r})$ represent the effects of pion absorption. In the early work B_0 was taken to be purely imaginary, but more recently B_0 has been taken to include corrections due to the nuclear medium and so becomes complex. In some recent work the factors $B_0 \rho^2(\underline{r})$ and $C_0 \rho^2(\underline{r})$ have been replaced by $4B_0 \rho_n(\underline{r}) \rho_p(\underline{r})$ and $4C_0 \rho_n(\underline{r}) \rho_p(\underline{r})$, respectively, since pion absorption is known to occur preferentially on neutron-proton pairs. The factor of 4 is included to facilitate direct comparisons with the results of earlier work.

To calculate the energy levels of the pion-nucleus system the complex non-local potential $V_N(\underline{r})$ must be introduced into the Klein-Gordon equation (Equation (5)). Theoretical predictions for the transition energies and level widths of pionic atoms can then be made using, for example, the computer code PIATOM (Krell, 1977). The potential V_e contains the effects of finite nuclear size and, if desired, of first order vacuum polarization. The potential V_N is used to find the complex energy eigenvalues $E_{n\lambda}$ of Equation (5) to an accuracy of one part in 10^6 .

$$E_{n\ell} = \text{Re}(E_{n\ell}) + \frac{i\Gamma_{n\ell}}{2} \quad (29)$$

where $\text{Re}(E_{n\ell})$ is the level energy and $\Gamma_{n\ell}$ the level width. In Chapter 5 the theoretical predictions and experimental results are compared and discussed.

Isotope Effects in Pionic Atoms

Since the optical potential contains terms depending explicitly on $\rho_n(\underline{r}) - \rho_p(\underline{r})$ it should be possible to extract the neutron radius difference

$$\Delta r_n = r_n(^{180}) - r_n(^{160})$$

from the π 16,180 isotope shifts

$$\begin{aligned} \epsilon_{1s}^{(180)} - \epsilon_{1s}^{(160)} \\ \Gamma_{1s}^{(180)} - \Gamma_{1s}^{(160)}. \end{aligned} \quad (30)$$

Previous experimental results have been included in global fits to pionic atom 2p-1s data to help determine optical model parameters more accurately. The 180 results are particularly valuable in this respect because of their sensitivity to the isovector part of the optical potential.

In ^{16}O , charge symmetry implies (neglecting Coulomb repulsion) that ρ_n is equal to ρ_p so that the isovector terms in the optical potential are nearly zero. Since the nuclear medium effects are almost the same in ^{16}O as in ^{18}O , the isotope shifts (Equation (30)) reflect almost entirely the effects of adding two neutrons to a closed shell. The isotope pair $^{20,22}\text{Ne}$ is also expected to provide valuable information on the isovector part of the optical potential and is currently under investigation (Li, 1985). One problem with the global fits is that the isovector parameters b_1 and c_1 can be determined only with the help of constraints on the size of the neutron distribution r_n , although it has been shown (Friedman, 1980) that it may be possible to determine simultaneously b_1 , c_1 and r_n within reasonable limits. In addition, the interrelated dependence of the optical potential on r_n and on the Lorentz-Lorenz parameter ξ (Powers et al., 1980) presents difficulties in the determination of r_n since the value of ξ is not well determined.

In the majority of analyses of the neutron density distribution in medium-Z nuclei the values of the parameters b_1 and c_1 were largely determined by the experimental results for the single isotope ^{18}O . It would appear that further

experimental information on isotope effects in $1s$ states is needed and the uncertainties in the values of the parameters b_1 and c_1 reduced before confidence can be gained in the use of pionic atom data to determine neutron density distributions.

CHAPTER 3

THE EXPERIMENTAL METHODIntroduction

The experiment consisted of stopping pions in ^{16}O and ^{18}O water targets and observing the resulting gamma and X-rays with an intrinsic germanium detector. The major objective of the experiment was to obtain a measurement of the values of ϵ and Γ in pionic ^{16}O and ^{18}O . The differences in ϵ and Γ between the two isotopes were then calculated and for this reason experimental conditions were kept almost identical when acquiring data with the two targets.

The experiment was performed at the TRIUMF M13 low energy pion and muon channel, shown in Figure 2. Pions are obtained when high energy protons strike the production target. To produce the proton beam H^- ions are injected into the centre of the TRIUMF cyclotron and accelerated to < 500 MeV where they are stripped of their electrons. The resulting proton beam, of up to $130 \mu\text{A}$, is then guided to a production target, via Beamline 1A. When the proton beam hits target nuclei, the following reactions, among others, may take place:

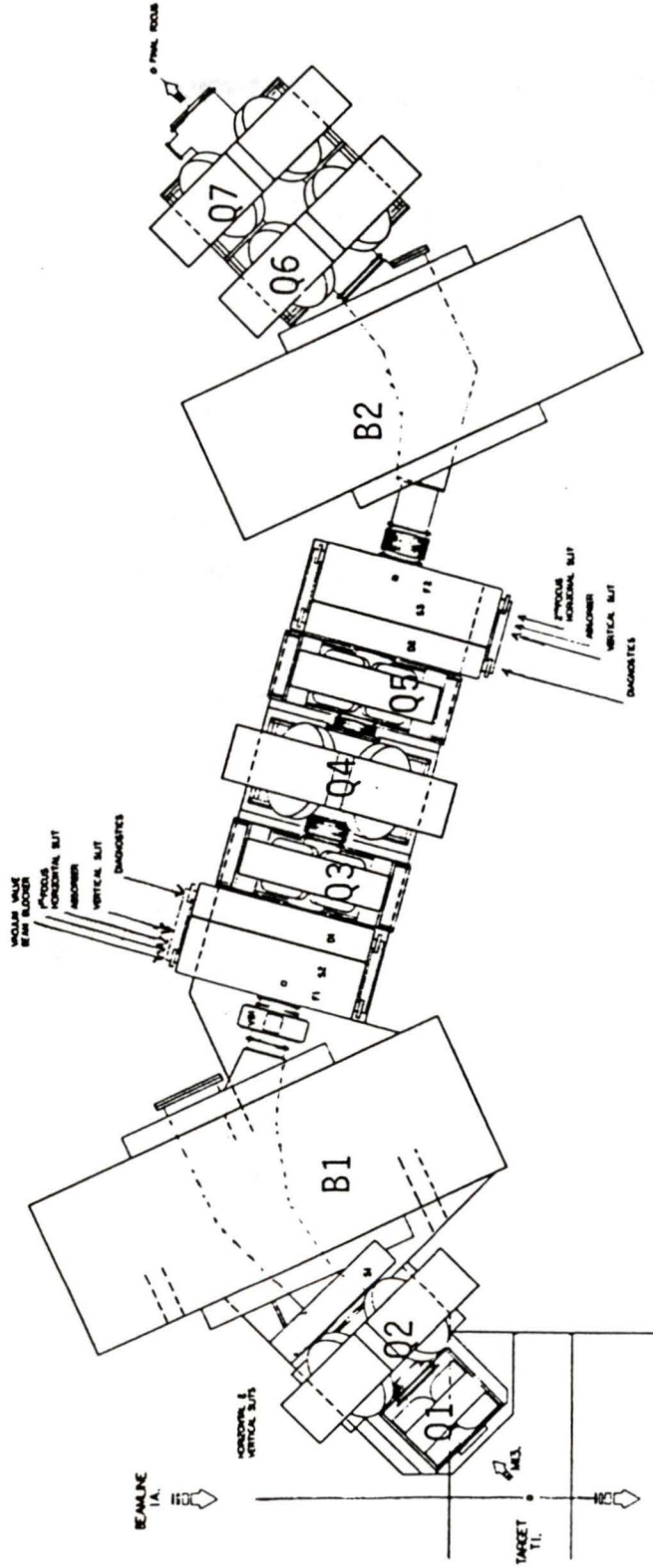
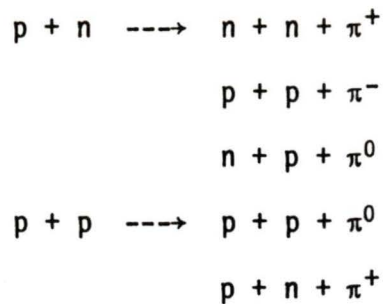


Figure 2: Arrangement of the M13 Channel



Conversion electrons from gammas from the decay of neutral pions are used to provide a relative measure of the proton flux in the primary beam line. Muons are produced near the target by pion decay.

At the energies of the pions produced (up to about 50 MeV), the pion production cross-section is approximately isotropic, (Mathie 1976) while the high energy neutrons that are produced are strongly forward peaked. To reduce the high energy neutron flux at the π focus, the M13 beam line views the production target at 135 degrees with respect to the primary proton beam. Focussing and bending magnets along the 9.5 metre channel collect the charged particles and deliver them as a beam at the final focal point, 60 cm from the exit of the final quadrupole, where the stopping target was located.

Experimental Arrangement

A four-scintillator telescope system was used to detect the incoming pions and define a stop event in the target. A particle stop in the target is defined by a signal in counters S1 and S2, but not in S3 and S4, i.e., 1.2.3.4. The experimental arrangement is shown in Figure 3. Scintillators S1 and S2 were 10 cm x 10 cm x 0.3 cm. Due to the presence of ^{16}O in S2, care was taken that it not be seen by the detection system. S3 was 14 cm x 14 cm x 0.4 cm and was placed directly behind the target to detect immediately any particles passing through the target before they could interact with oxygen in the air. To detect particles which passed through S1, S2, S3 and the target the second anti-counter, S4, was chosen to be larger (20 cm x 20 cm). In addition, it was kept far downstream to avoid false counts due to particle emission from the target after a π -stop. All counters were wrapped by aluminized mylar tape rather than black tape, which contains polyvinylchloride (PVC). The 3d-2p pionic X-ray of chlorine, known to be a contaminant in previous $\pi^{16,18}\text{O}$ experiments was due to the PVC in the black tape.

A beryllium degrader of thickness 1.85 g/cm^2 was placed between S1 and S2 to increase the number of pions stopping in

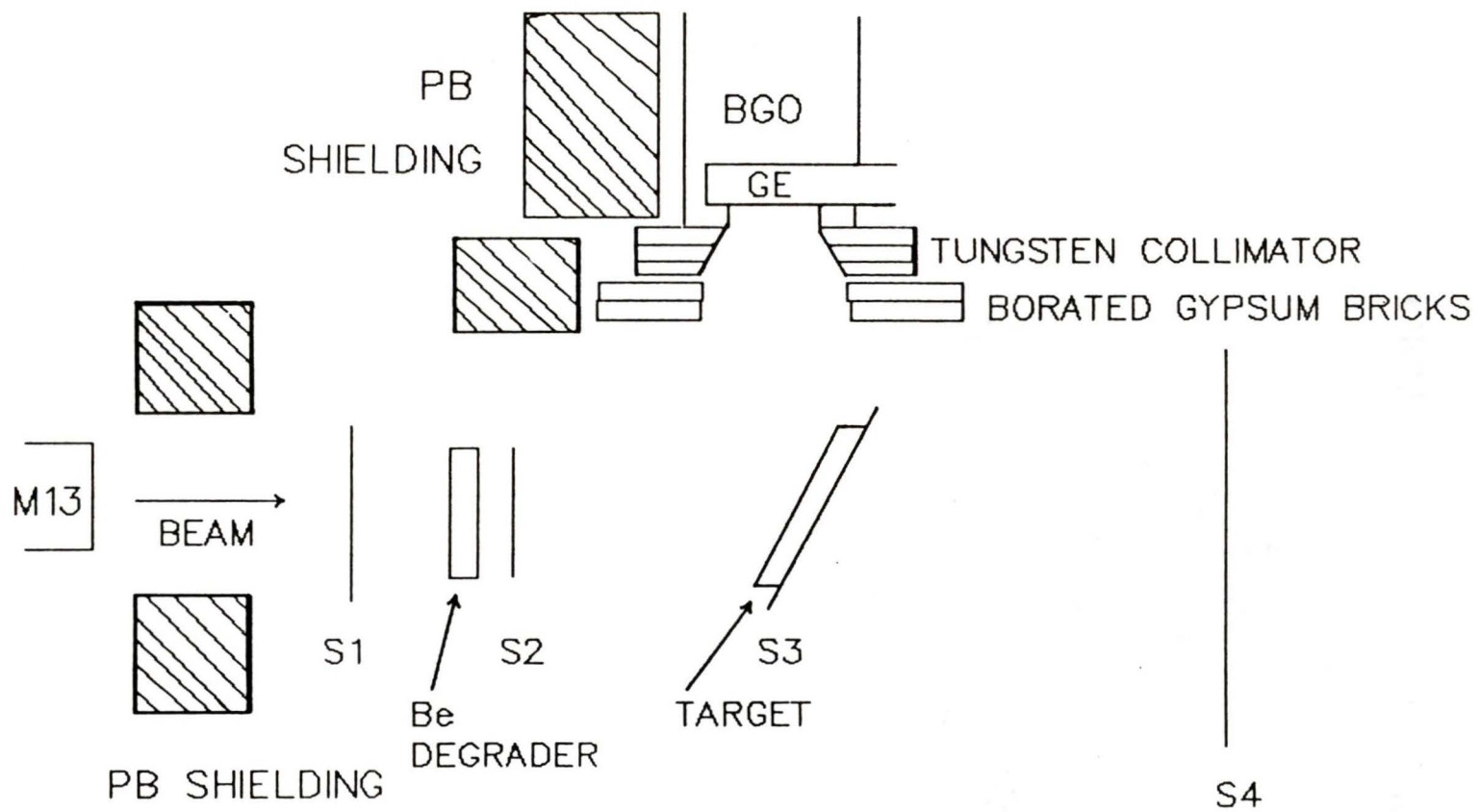


Figure 3: Experimental Arrangement

the target. Simply setting the channel momentum lower would have resulted in a lower flux of pions at the target. A particle stopping in the degrader was identified by a 1.2 signal; beryllium was chosen since its muonic and pionic X rays are outside the energy region of interest in this experiment.

The momentum of the M13 channel is 20-130 MeV/c. The channel momentum was initially set at 88 MeV/c and then fine-tuned during the course of the experiment to optimize the stopping rate of pions in the target. This was done by plotting the relative number of stops as defined by the ratio 1.2.3.4 to 1.2 (see Figure 7) versus the channel momentum. The channel momentum was changed by adjusting the currents in the bending magnets B1 and B2, and in the quadrupoles Q1 through Q7 shown in Figure 2. Adjusting the current by a certain percentage caused an equivalent change in the channel momentum.

Pions were distinguished from other particles stopping in the target by their time-of-flight along the channel. The momentum acceptance ($\Delta p/p$) of the channel is controlled by sets of horizontal slits in the channel. Because all transmitted particles have nearly the same momentum, particles of the same mass arrive at the target at

approximately the same time. Electrons, since they are the least massive, arrive first, followed by the muons and then the pions (see Figure 4). At the momentum setting used in this experiment, the pions, electrons and muons arrived at the experimental area in distinct groups. Muons, which come from the decay of pions along the channel have a greater spread in momentum for a given horizontal slit opening than do the pions or the electrons. The momentum of the muons coming from forward pion decays overlaps the momentum distribution of the pions, making it impossible to totally separate them by time-of-flight.

Both the ^{16}O and ^{18}O targets were liquid. The ^{16}O target consisted of distilled water while the specified isotopic

1)
purity for the H_2^{18}O target was

^{18}O : 98.0 %

^{17}O : 0.5 %

^{16}O : 1.5 %

The front of the X-ray detection system was located about 40 cm from the beam axis and was shielded with about 4 cm of Densimet collimator (a tungsten alloy). The beamline side of the detection system was shielded with lead bricks and the

1)

Manufactured by Los Alamos Meson Production Facility.

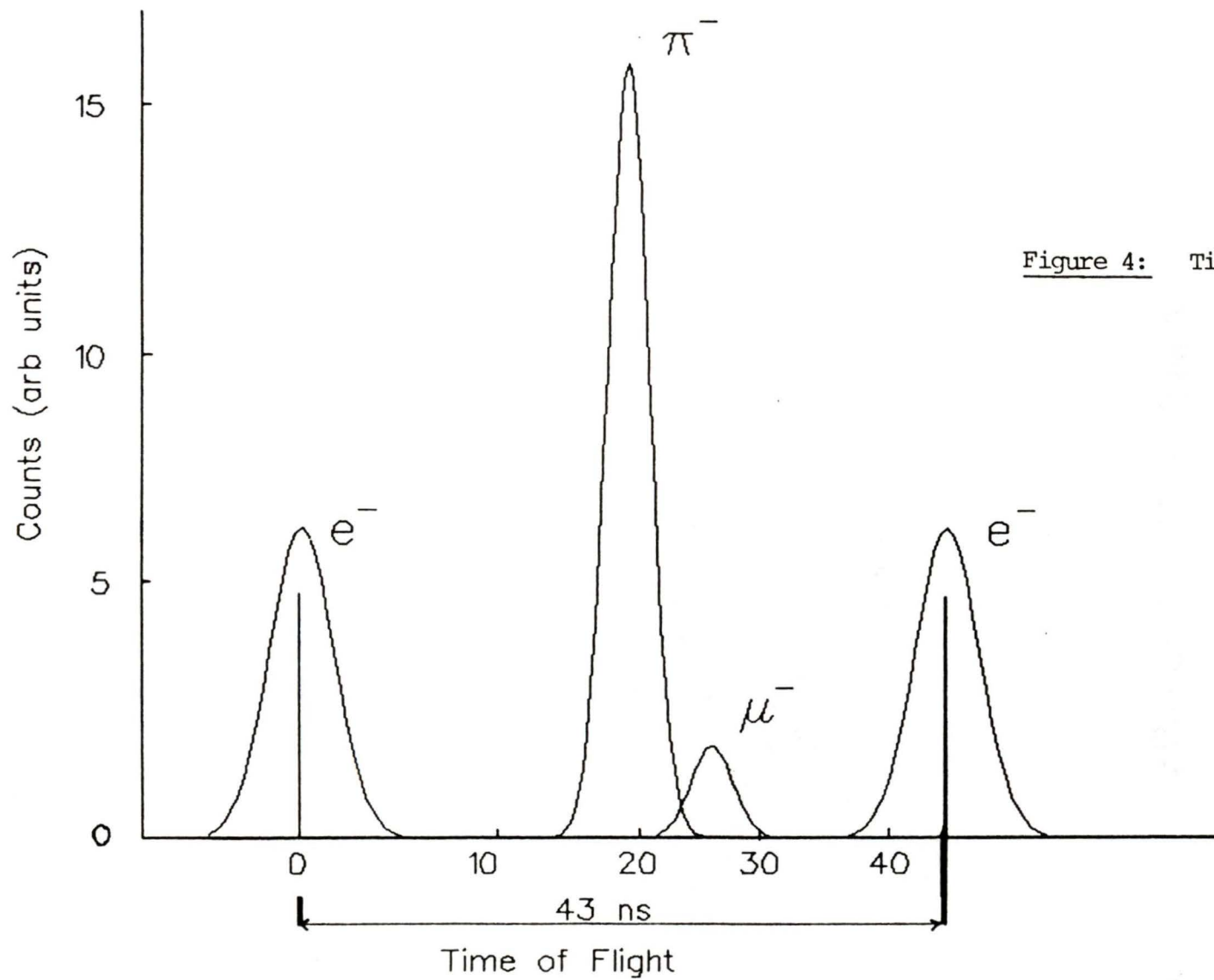


Figure 4: Time-of-Flight Spectrum

system was also shielded with borated gypsum bricks in an effort to moderate high energy neutrons, which rapidly cause radiation damage to a germanium detector.

The X ray Detection System

The detection system consisted of a Princeton Gamma-Tech hyperpure germanium detector, surrounded by a bismuth germanate²⁾ (BGO) Compton suppression system. The purpose of the suppressor system is to reduce the background due to the Compton scattering of photons in the Ge detector. A photon Compton scattered from the Ge detector will be detected in the BGO and this signal can then be used to veto the original signal in the germanium detector. For a description of the construction and operation of the BGO system, see Olin et al. (1984). A brief description is given here. The spectrometer is constructed out of sixteen 5.5 x 5.5 x 8.0 cm BGO crystals, arranged as four pairs in each half of an aluminum shell. The arrangement is shown in Figure 5. Photons enter through a hole in one end of the assembly, and the Ge detector is inserted in a hole perpendicular to the photon entrance hole.

2)

Chemical Symbol $\text{Bi}_4\text{Ge}_3\text{O}_{12}$.

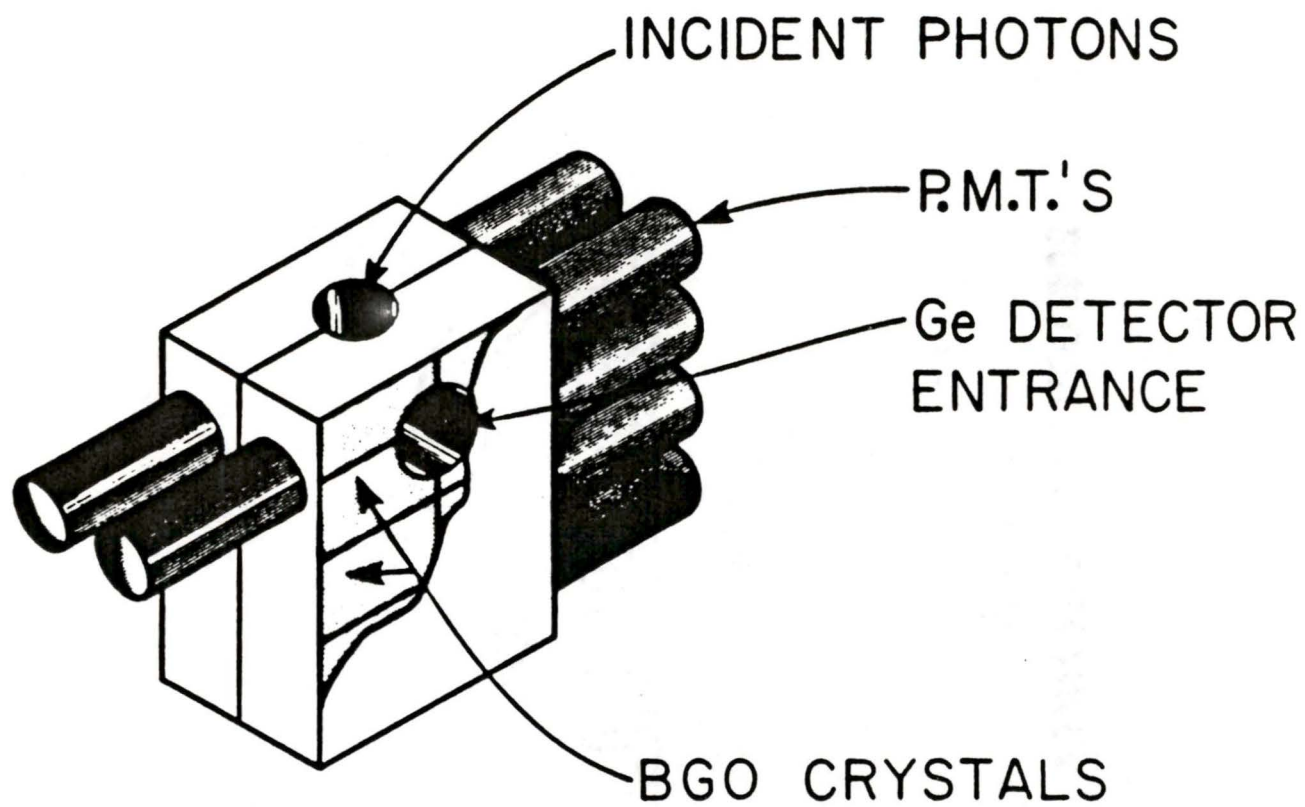


Figure 5: BGO Compton Suppressor

Each pair of crystals is isolated from the rest but optically coupled together and viewed from one end by a 5 cm diameter photomultiplier tube (PMT). Backscattered photons have the lowest energy; therefore, to adequately detect these photons the front pair of crystals in each half is viewed from both sides. The geometry of the Compton suppressor is such that the Compton edges of unsuppressed spectra are converted to broad peaks that can be approximated by a Lorentzian lineshape.

A good description of the design and operation of a high purity germanium detector is given by, for example, Goulding and Pehl (1974). A few important points are briefly discussed here. The ionization produced in the detector material should be linearly proportional to the energy of the incoming photon. The number of electron-hole pairs produced by the incoming photon should be large, to minimize any statistical fluctuations. When a bias voltage is applied across the crystal these electrons and holes are collected at the electrodes. The electron-hole pairs should be highly mobile with a low probability of trapping or recombination so that they can be collected within a reasonable time, with little or no leakage current. The most common materials satisfying these requirements are germanium and silicon. Since the photoelectric effect is the primary absorption mechanism in the energy region up to about 100 keV, and proportional to

Z^5 , germanium with its higher Z is much more efficient for detecting X-rays. The total charge of the output signal will be proportional to the full energy of the incident photon unless the photon Compton scatters out of the crystal; it is this type of event that the BGO system is designed to suppress. At room temperature large numbers of electron-hole pairs are produced by thermal excitation of electrons across the 0.7 eV band gap of germanium, so in order to detect signals from incoming photons it is necessary to cool the detector with liquid nitrogen to 77 K.

There are two main contributions to the resolution of a germanium detector in the energy region of interest in this experiment: the electronic noise in the external amplifying circuit and the statistical nature of the electron-hole pair production and charge collection processes in the detector. These two effects add in quadrature to give the FWHM (full width at half maximum) or resolution of the resulting spectral line. Resolution of a particular detector is determined experimentally (see Chapter 4).

One of the major concerns when using a solid state Ge detector is that of damage caused by radiation. The most damaging form of radiation is fast neutrons since they lose energy by nuclear collisions with the Ge nuclei rather than by ionization. These collisions result in crystal

dislocations which lead to poorer resolution and the presence of an excess of counts in the spectrum on the low energy side of the peak, referred to as a low energy tail. This tail is due to charge trapping at impurities and defects in the crystal lattice. Parameters describing the tailing are also determined experimentally (again, see Chapter 4).

The Data Acquisition System and Electronics

A PDP 11/34 computer connected via a CAMAC interface to the experiment was used for the data acquisition. A complete schematic drawing of the circuit logic is shown in Figure 6. The circuit logic can be divided into 4 sections: the scintillator telescope logic, the germanium detector logic, the BGO suppressor logic, and the trigger logic.

Whenever the trigger received a signal that an event was detected in the germanium counter, the BGO suppressor and scintillator telescope sections of the logic were examined. If the event was not vetoed by the suppressor and satisfied either the 'target stop' or 'source event' requirements in the telescope logic, a trigger pulse was formed. While each event was being recorded on magnetic tape the trigger was disabled, and upon completion the system was reset to accept another event.

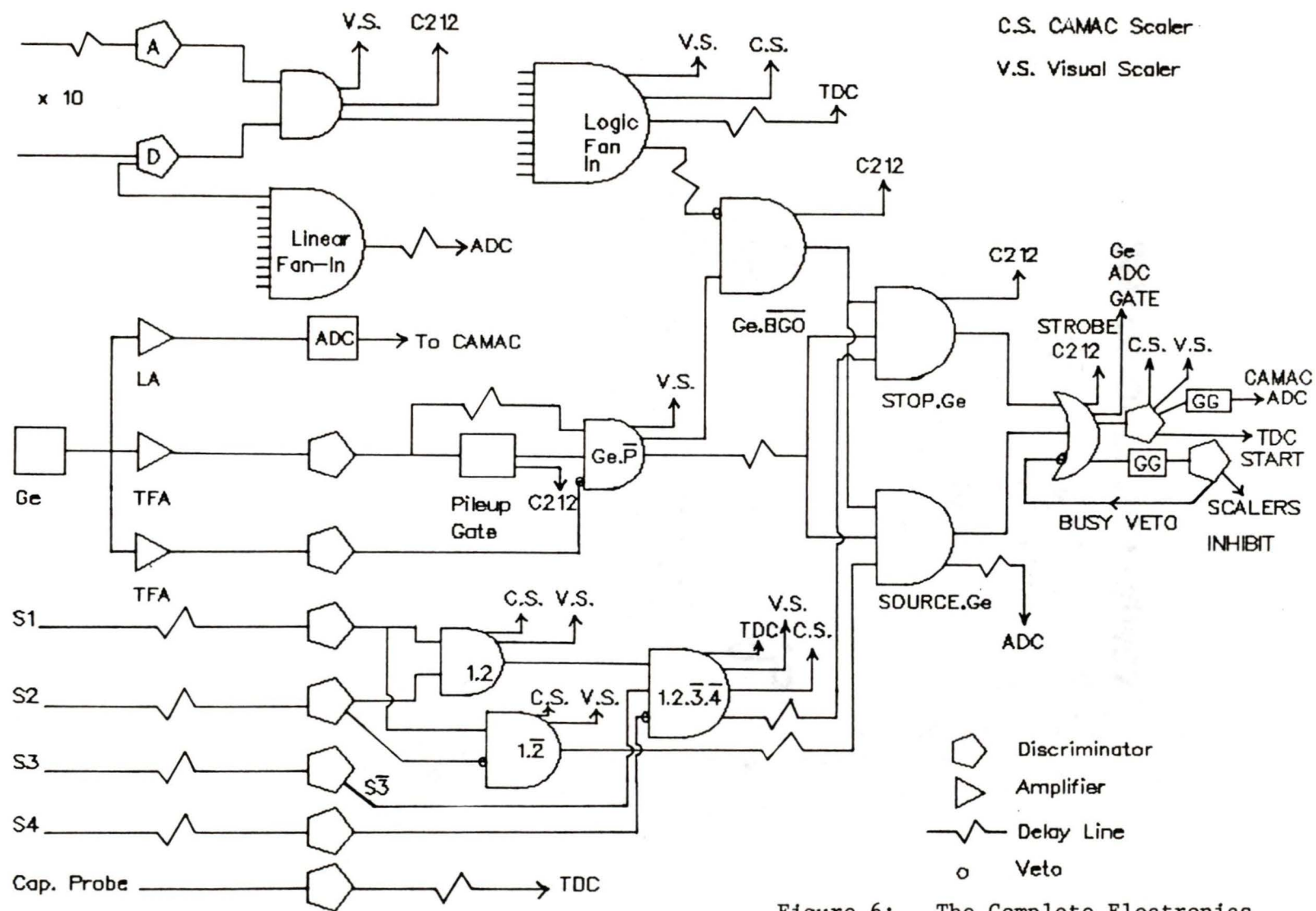


Figure 6: The Complete Electronics

In an attempt to reduce the contribution from muons stopping in the target, a capacitive probe was used to monitor the time of arrival of protons at the production target. Every 43 nanoseconds (ns) a bunch of protons would strike the production target and a signal which passed from the probe, through a discriminator, to a time-to-digital converter (TDC) was used to record the timing of particle production relative to a stop in the target. In this way a time-of-flight spectrum (see Figure 4) was obtained and appropriate software timing cuts chosen to reduce the contribution to the prompt spectrum from muons stopping in the target. This requirement was added just before the end of the π^{180} portion of the experiment so that approximately 15% of the π^{180} data and all of the π^{160} data were collected with the time-of-flight condition included.

Scintillator Telescope Logic

This section of the electronics (shown in Figure 7) produces two gate pulses used to define events to be recorded by the data acquisition system. A pion stop in the target was defined by a $1.2.\bar{3}.\bar{4}$ coincidence while a $1.\bar{2}$ signal corresponded to a stop in the degrader. The latter coincidence was used to define a source event and when this

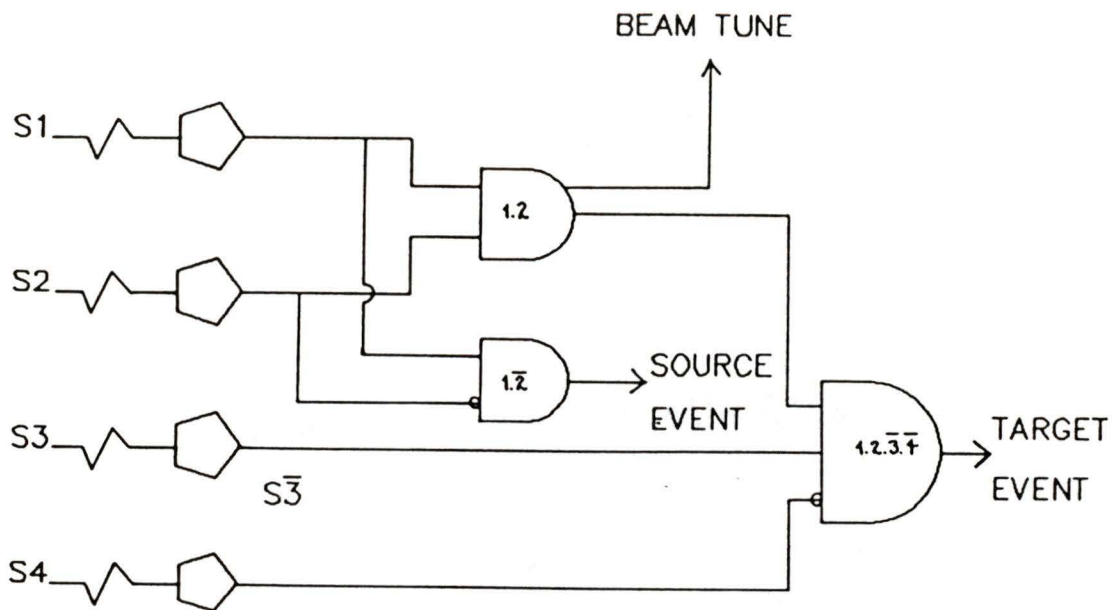


Figure 7: Scintillator Telescope Logic

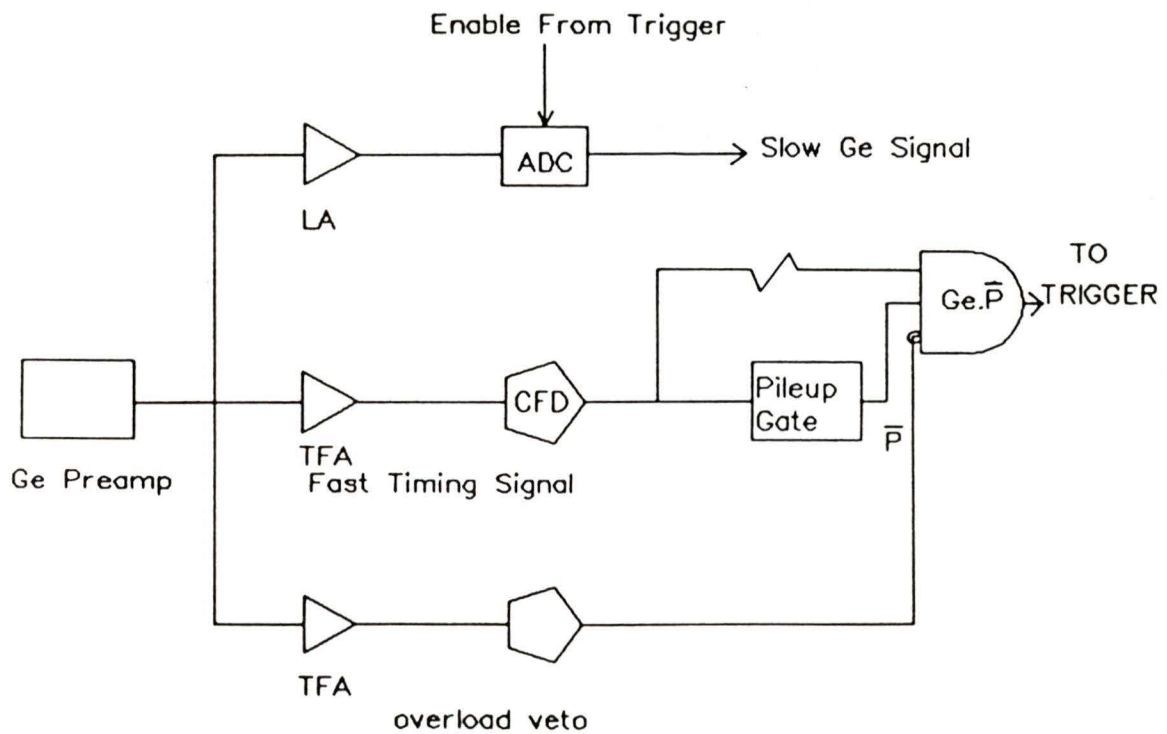


Figure 8: Ge Detector Logic

condition was met, data were recorded under beam conditions from radioactive sources located near the detector. All events within 100 ns of a stop in the target were recorded. The width of the gate pulse for a source event was set so that the target and source event rates were about equal.

Germanium Detector Logic

This section of the electronics (shown in Figure 8) began with a FET preamplifier which integrated and shaped the output signal of the detector corresponding to a photon received in the detector. The signal was then sent to two branches: a linear branch and a fast timing branch.

In the slow linear branch, the Ge preamplifier signal was fed to a linear amplifier where it was shaped and amplified. The amplified signal was then directed to an analog-to-digital converter (ADC) where its energy-dependent amplitude was converted to a digital code. The fast germanium timing signal was obtained by passing the Ge preamp signal to a timing filter amplifier (TFA) where it was differentiated and amplified and then sent through a constant fraction discriminator (CFD). The CFD output timing signal was nearly independent of the amplitude of the original signal.

The fast timing branch was then split into two branches;

the first branch went to a pileup gate and the second was delayed. The pileup gate rejected any signal if it followed a previous pulse within the time ($\sim 10 \mu\text{s}$) required by the Ge detector system to fully process a signal. A coincidence was formed between the no-pileup signal and the delayed signal, and this carried the timing of the original event in the detector. The signal from the preamplifier was also sent through a third branch consisting of a second TFA and a discriminator with a high threshold in order to reject pulses that corresponded to a very high energy.

BGO Logic

The BGO logic (shown in Figure 9) was duplicated for each of the 10 segments of the suppressor. Each segment was instrumented separately to allow for high rate capabilities under beam conditions. For each segment a coincidence was required between a discriminator dynode signal and a suitably delayed anode discriminator signal. The anode signal was delayed until nearly the end of the dynode signal, and an 80 ns veto pulse was formed if a coincidence existed. Such a coincidence in any of the ten segments defined an event in the BGO which was then used to veto the corresponding event in the Ge detector.

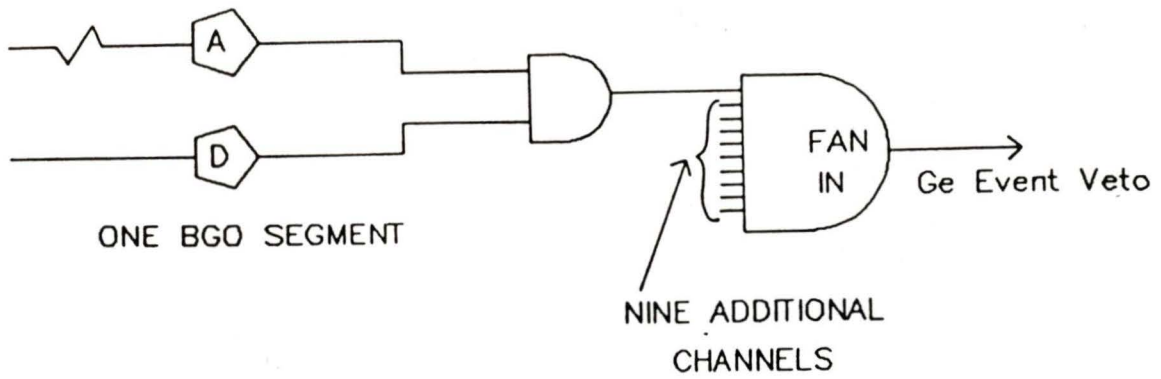


Figure 9: BGO Logic

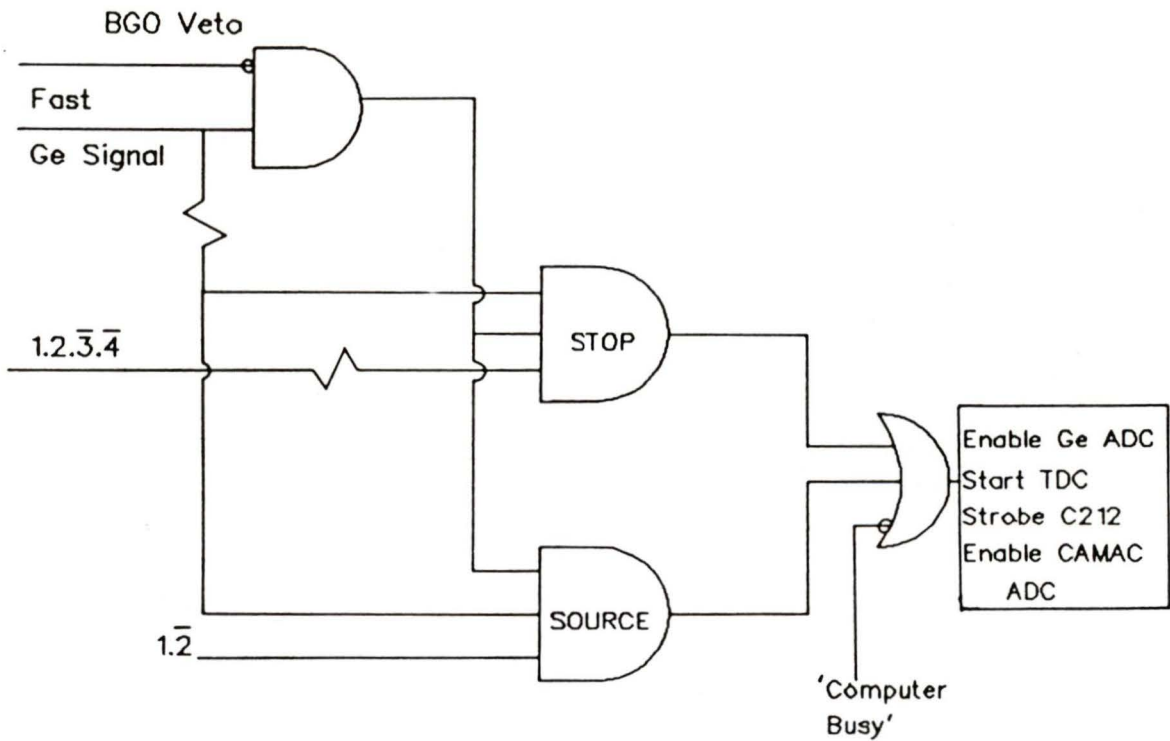


Figure 10: Trigger Logic

Trigger Logic

This section of the circuit (shown in Figure 10) was used to sort the events into source and target related events. If there was no veto signal from the BGO and the 'clean' (no pileup and no overload) fast Ge signal, suitably delayed, was in coincidence with a stop or source event in the telescope logic, a trigger signal was formed.

The trigger signal was used for a number of purposes. It was used to gate the ADC so that the energy information carried by the slow Ge signal could be digitized. It was also used to strobe the C212 pattern register unit that recorded whether an event was a source event or a stop event. A time-to-digital converter (TDC) was also started by the trigger and stopped by the fast Ge timing signal. This timing spectrum showed the time of the event in the germanium detector relative to the time of the stop in the target and was used to define prompt and delayed energy spectra.

The trigger was also sent to the computer to enable processing of the event to begin. While the computer was recording an event the trigger was vetoed.

CHAPTER 4

DATA ANALYSISIntroduction

Three types of spectra were acquired from data recorded on tape during the experiment: an energy spectrum associated with a π -stop in the target, an energy spectrum associated with a source event, and timing spectra. The timing spectra were of two types: a time-of-flight spectrum based on the different arrival times of pions, muons and electrons at the experimental target and a spectrum associated with the timing of the pulses in the Ge detector with respect to a pion stop in the target.

The prompt spectra contained the 2p-1s X-ray lines and the goal of the analysis was to find the energies and widths of these X rays. By plotting energy versus the timing information, suitable software cuts were chosen to separate the target events into prompt and delayed spectra thereby reducing the background in the prompt spectrum. The time-of-flight spectra were used in an attempt to reduce the intensity of the muonic lines in the prompt spectra.

The ^{180}O data were separated into two different sets for separate analysis (referred to as Data Sets I and II) because of a problem with drifts in the energy stabilization system. The ^{160}O data which did not appear to be significantly affected by stabilizer problems are referred to as Data Set III. The two sets of ^{180}O data were analyzed independently and the results averaged.

The source spectra from the individual data sets were used to obtain information about the detector resolution while source spectra recorded with ^{57}Co and ^{133}Ba sources with the target empty were used to determine the low energy tailing parameters and detector efficiency. Well-defined peaks in the prompt and source spectra of each data set were used for energy calibration.

The Peak Fitting Program

The data were analyzed with a gamma ray fitting program, JAGSPOT, developed at Chalk River and modified to fit Lorentzian-broadened pionic X rays (Olin, 1978). The experimental spectrum is fitted to a function $\phi(x_i, \bar{a}_i)$ where the \bar{a}_i describe the background, lineshape, peak intensities

and tailing. The general form of the lineshape fitting function is

$$\phi(x_i, \bar{a}_i) = a_1 + a_2 x_i + b(x_i) + \sum_{j=1}^N a_{2j+3} f_{\alpha_j}(x_i - a_{2j+4}) \epsilon(x_i) \quad (31)$$

where x_i is the channel number, $\epsilon(x_i)$ is the detector efficiency function, $b(x_i)$ the tailing function, and f_{α_j} is the lineshape function for the N 'th peak. Up to 10 peaks in a maximum allowed region of 500 channels may be fitted simultaneously and the peaks may be either Gaussian, or a convolution of the Gaussian with one of three Lorentzians with differing FWHM values. A least-squares fitting method is used to obtain the best values of the parameters \bar{a}_i , as judged by a minimum in the variable χ^2 , and the a_i can be fixed or allowed to vary.

The first three terms in Equation (31) describe the background. The term $b(x_i)$ describes the peak asymmetry due to the low energy tailing

$$b(x_i) = a_{25} \sum_{j=1}^{N_{\text{chan}}} (y_j - d_j) e^{-a_{26} (x_j - x_i)} \quad (32)$$

There are also provisions in the program for an exponential background

$$a_1 \exp(-a_2 x_i) \quad (33)$$

or a step background

$$s(x_i) = a_{27} \sum_{j=1}^{N_{\text{chan}}} \{y_j - [a_1 + a_2 x_j + b(x_j)]\} \quad (34)$$

where y_j is the number of counts in channel j , N_{chan} the number of channels, and d_j the background, given by

$$d_j = a_1 + a_2 x_j + b(x_j). \quad (35)$$

The detector efficiency depends on the experimental conditions and past history of the detector and must be determined for each experimental measurement. Measured efficiencies are fit to an appropriate function which is then included in the fitting program. The relative efficiency may then be normalised to 1.0 at the centre of the fit region. The correction due to detector efficiency is then applied to

the broadened Lorentzian lineshape since relative efficiency varies over the peak width.

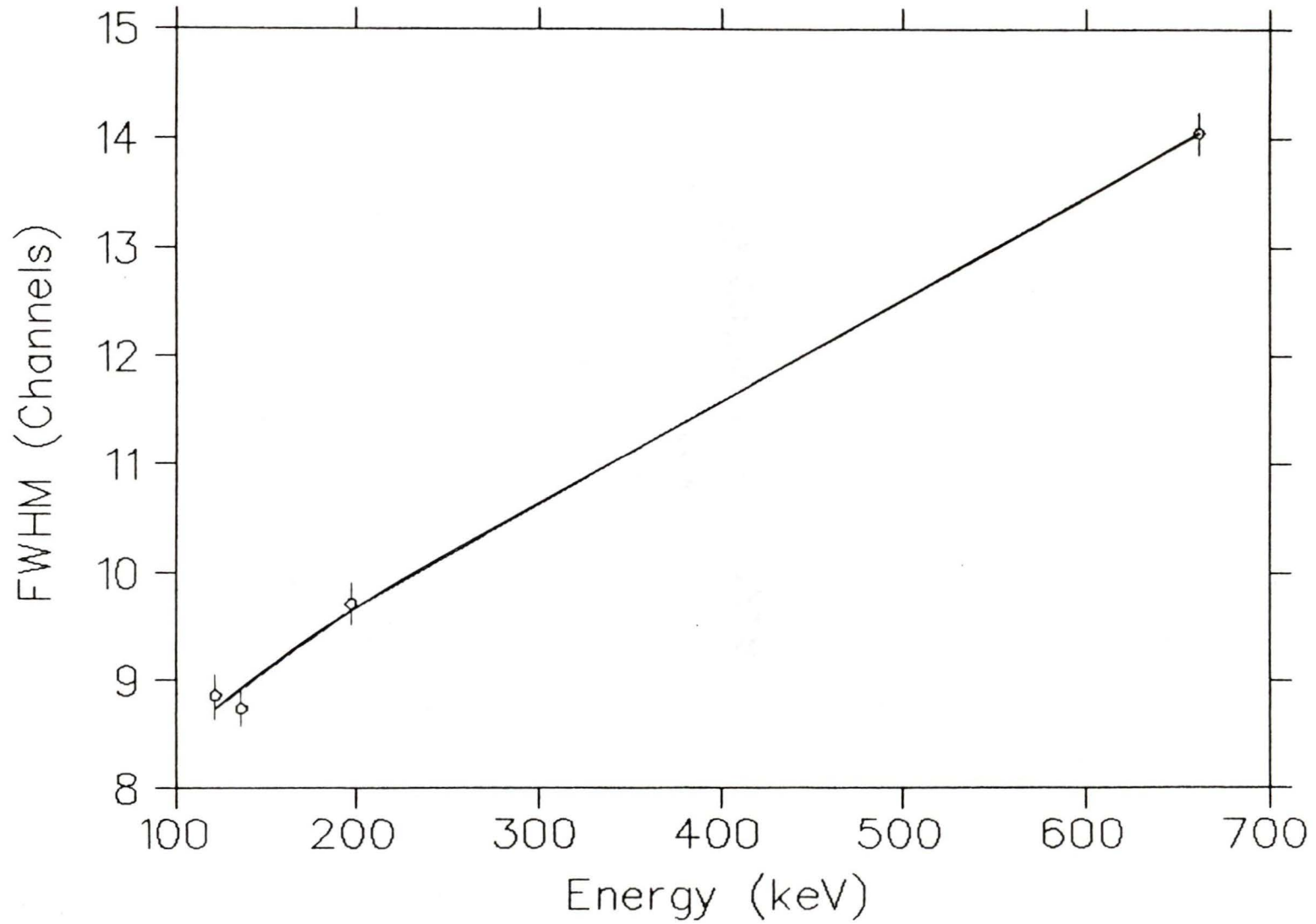
The Detector Response Function

The detector response function consists of three components: energy resolution, low energy tailing and detector efficiency as a function of energy. The resolution was determined for each data set by fits to several gamma ray lines in the source spectrum (see Figure 11) of that data set. This was done because of possible broadening of the lineshapes due to drifts in the energy stabilization system and expected worsening of the resolution as the experiment progressed due to radiation damage. The resolution was obtained by fitting the FWHM of these peaks to the following expression

$$(\text{FWHM})^2 = a_1 + a_2 E \quad (36)$$

where a_1 is the contribution of electronic noise in the external circuit and a_2 is due to statistical processes in the detector. The FWHM at 158 keV for the three sets of data were found to be:

Figure 11: Resolution as a Function of Energy



$$\begin{aligned} \pi^{18}\text{O}: \text{ Set I} & \quad 1.146(0.035) \text{ keV} \\ & \quad \text{Set II} \quad 1.121(0.038) \text{ keV} \\ \pi^{16}\text{O}: \text{ Set III} & \quad 1.165(0.041) \text{ keV} \end{aligned}$$

The detector efficiency function was obtained by fitting the measured intensities of six ^{133}Ba and two ^{57}Co gamma ray peaks in the source spectrum (see Figure 12) to the following function

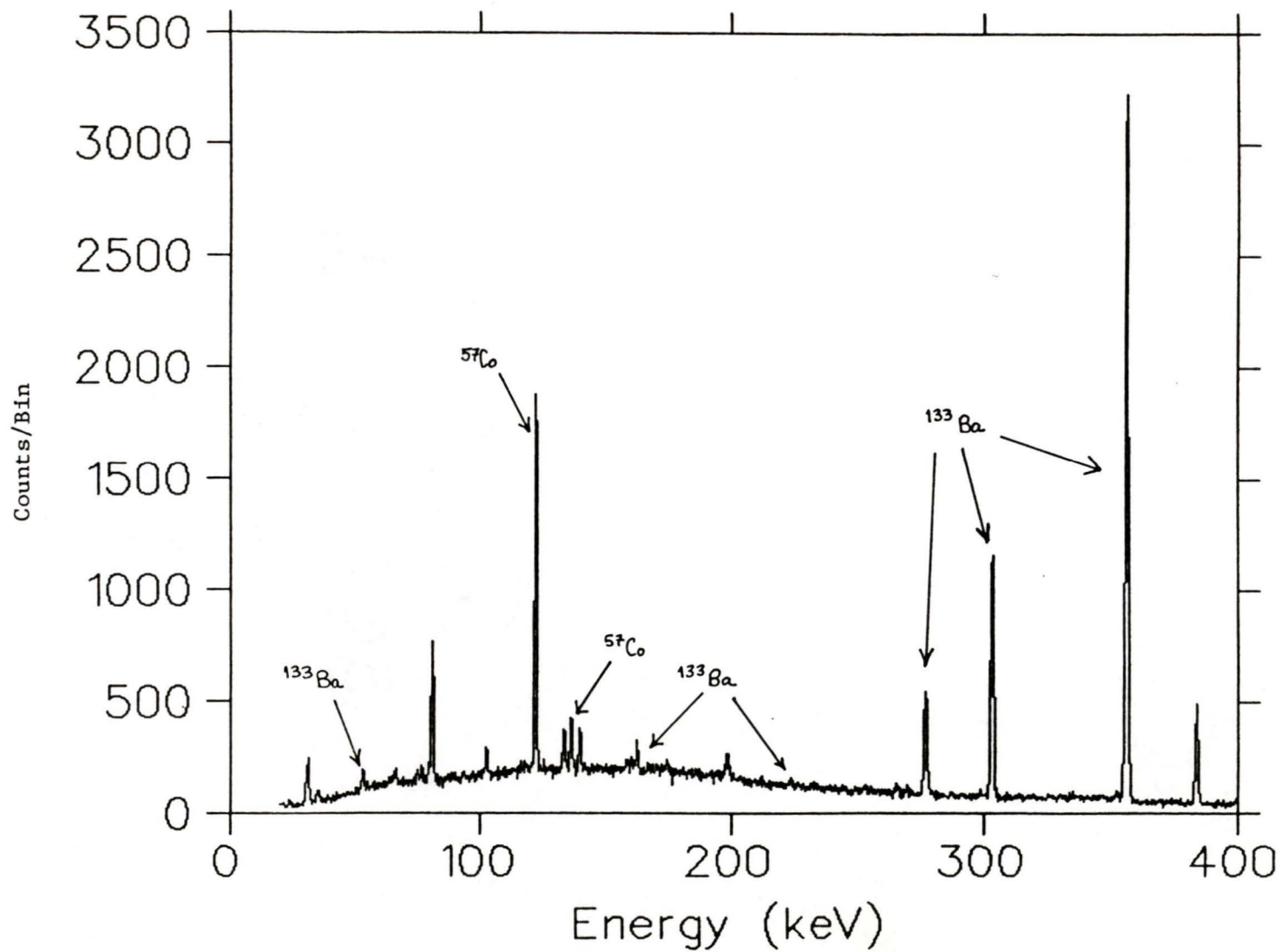
$$\begin{aligned} \epsilon(E) = c_1 e^{-c_4(x_{\text{photo}} + x_{\text{incoh}})} & \quad (37) \\ \times \left(1 - e^{(-c_2 * x_{\text{photo}} - c_3 * x_{\text{incoh}})} \right) \end{aligned}$$

where $x_{\text{photo}} = 339000 \cdot x E^{-2.97}$ is the photoelectric cross-section and

$$x_{\text{incoh}} = \begin{cases} 0.1245, & E < 81 \text{ keV} \\ 0.1334 - 0.0001313 \times E, & E > 80 \text{ keV} \end{cases}$$

is the incoherent scattering cross-section for germanium (units in cm^2/g and E in keV). These relationships were based on data given in Storm and Israel (1970) and are valid from 50 to 350 keV. The measured intensities, $I(E)$, were combined with the relative intensities of Mayer (Table

Figure 12: Ba/Co Source Spectrum



of Isotopes, 7th Edition), $I_R(E)$, to define the relative efficiency $\epsilon(E)$ of the detector at energy E ;

$$\epsilon(E) = I(E)/I_R(E).$$

The different strengths and intensities of the two sources were included in the calculation of the relative efficiency. The peaks used, and their intensities, are shown in Table 1.

The values of $\epsilon(E)$ were fit to the functional form given by (37) and the 'best-fit' function, shown as a solid line on Figure 13, had parameters $c_1 = 44.3 \pm 0.3$, $c_2 = 147.9 \pm 3.8$, $c_3 = 4.1 \pm 0.4$ and $c_4 = 0.21 \pm 0.03$. The function $\epsilon(E)$ was then normalized to 1.0 at the centre of the fitting region. The function minimization and analysis package MINUIT (James and Roos, 1975) was used for this analysis.

Figure 13: Relative Efficiency from Barium and Cobalt Sources

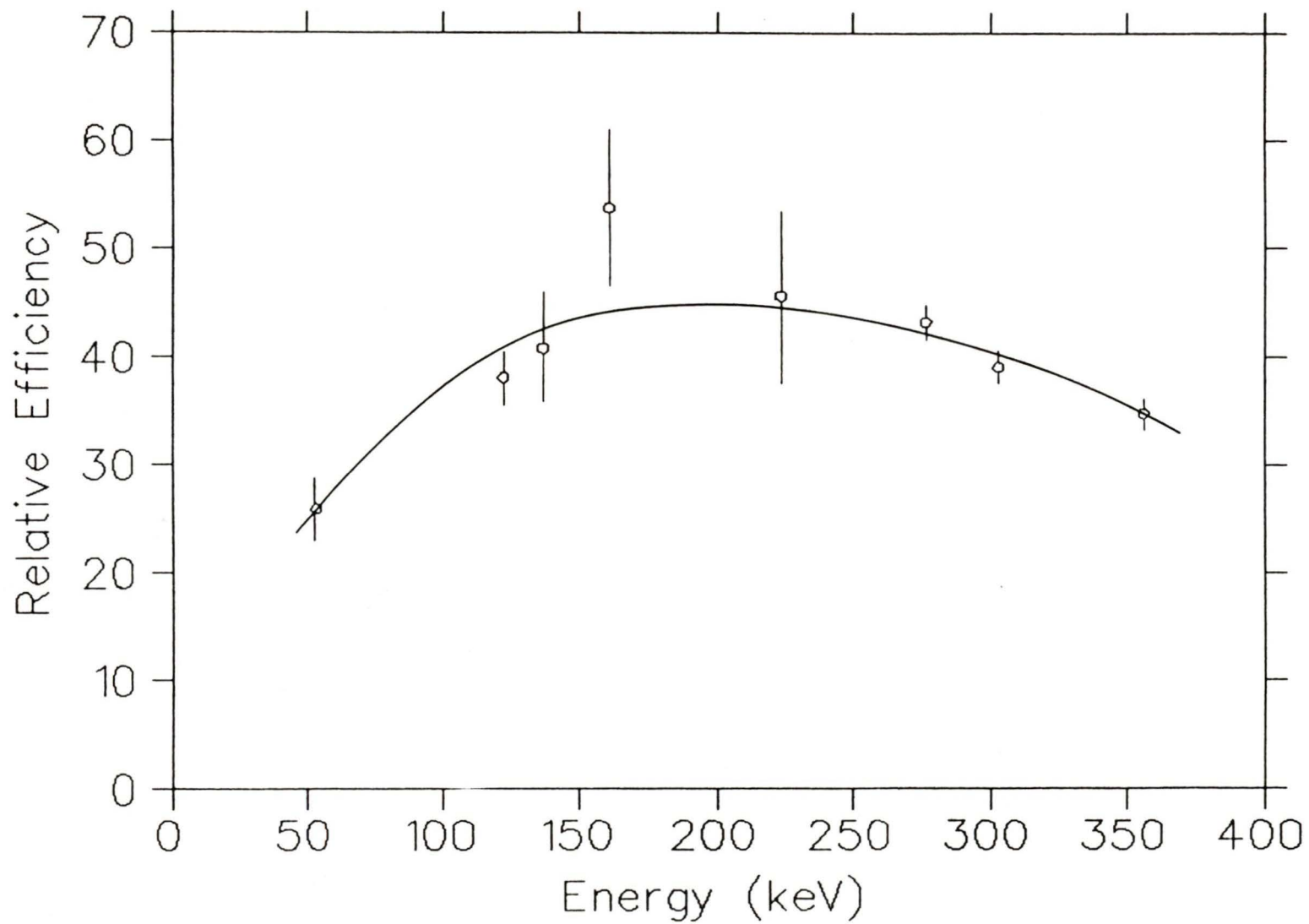


Table 1 Peaks Used to Determine
Detector Efficiency

Peak	Energy (keV)	Measured Intensity	Relative Intensity
^{133}Ba	53.156(0.005)	902(61)	34.8(0.7)
^{57}Co	122.06135(0.00013)	15551(153)	725
^{57}Co	136.47434(0.00030)	2168(78)	94.3(2.9)
^{133}Ba	160.609(0.025)	564(60)	10.5(0.3)
^{133}Ba	223.116(0.035)	324(49)	7.1(0.2)
^{133}Ba	276.404(0.007)	4876(83)	113 (2)
^{133}Ba	302.858(0.005)	11426(118)	292 (3)
^{133}Ba	356.014(0.009)	34771(226)	1000 (3)

The parameters of the low energy tailing function, obtained by fitting gamma ray peaks in the source spectra, are tabulated in Table 2. The tailing is described by two parameters, a_{25} , the amplitude of the tail, and a_{26} , the reciprocal of the range of the tail. In most cases the peak statistics were not high enough to determine both tailing parameters simultaneously, so a procedure in which each parameter was alternately fixed and floated was adopted.

In the final analysis the uncertainty in the tailing parameters was assumed to range from zero to the final chosen values. The case of $a_{25} = a_{26} = 0$ corresponded to a very long range tail and was taken into account with a small positive step background. The uncertainty in the tailing parameters was found to have a significant effect on the widths of the broadened pionic X rays and contributed to the error in the final result.

Table 2 Tailing Data

Gamma Ray Energy	a_{25}	a_{26}
122 keV	0.00124(0.00036)	0.01710(0.01510)
197 keV	0.00163(0.00056)	0.03049(0.01389)
276 keV	0.00097(0.00081)	0.01632(0.01031)
302 keV	0.00070(0.00060)	0.01290(0.01130)
356 keV	0.00069(0.00006)	0.00766(0.00127)

The tailing parameters used in the analysis were:

$$a_{25} = 0.00124 \quad a_{26} = 0.01689$$

Energy Calibration

The most accurately known peak positions in both source and prompt target event spectra were used to determine the energy calibration. An energy calibration was done separately for each set of data using the gamma rays given in Tables 3-5.

Table 3 Energy Calibration Peaks (Set I)

Peak	Energy (keV)	Channel	Fit Energy
^{57}Co	122.06135(0.00013) ¹	1006.40(0.10)	122.070(0.012)
^{57}Co	136.47434(0.00030) ¹	1125.13(0.12)	136.471(0.015)
$\mu^{18}\text{O}$ 2-1	133.553(0.016) ²	1101.05(0.10)	133.550(0.019)
e^+, e^-	511.003(0.001)	4213.04(0.15)	510.990(0.018)
^{137}Cs	661.661(0.003) ¹	5455.41(0.10)	661.671(0.012)

Table 4 Energy Calibration Peaks (Set II)

Peak	Energy (keV)	Channel	Fit Energy
$\mu\text{N } 2-1$	102.406(0.015) ³	845.65(0.18)	102.419(0.026)
^{57}Co	122.06135(0.00013) ¹	1007.60(0.10)	122.064(0.012)
^{57}Co	136.47434(0.00030) ¹	1126.33(0.13)	136.467(0.016)
$\mu^{18}\text{O } 2-1$	133.553(0.016) ²	1102.22(0.10)	133.544(0.019)
e^+, e^-	511.003(0.001)	4213.92(0.15)	511.007(0.018)
^{137}Cs	661.661(0.003) ¹	5455.85(0.10)	661.659(0.012)

Table 5 Energy Calibration Peaks (Set III)

Peak	Energy (keV)	Channel	Fit Energy
$\mu\text{N } 2-1$	102.406(0.015) ³	843.81(0.18)	102.414(0.026)
^{57}Co	122.06135(0.00013) ¹	1005.80(0.10)	122.059(0.012)
$\mu^{16}\text{O } 2-1$	133.525(0.015) ²	1100.27(0.10)	133.516(0.019)
e^+, e^-	511.003(0.001)	4213.07(0.15)	511.012(0.018)
^{137}Cs	661.661(0.003) ¹	5455.26(0.10)	661.655(0.012)

(1) Table of Isotopes, 7th Ed.

(2) Backenstoss et al. (1980).

(3) Engfer et al. (1974).

The energies of the gamma rays versus channel position were fit to both linear and quadratic functions using a standard least-squares method. In all three cases the quadratic term was small (of the order of 10^{-9}) and so the linear calibration was used. Figure 14 shows the differences between the known gamma ray energies and the fitted energies for all three data sets.

Since there is a large gap between the gamma rays at 122 keV and 511 keV, non-linearities were investigated using the positions of the ^{133}Ba and ^{57}Co peaks (those from Table 1). No significant non-linearities were found.

The results of the fits were:

$$E = a_1 + a_2 \times \text{channel} \quad (38)$$

$$\begin{aligned} \pi^{180}: \text{Set I} \quad a_1 &= 0.0076(143\%) \\ &a_2 = 0.121285(0.003\%) \\ &\text{Set II} \quad a_1 = -0.1615(6.5\%) \\ &a_2 = 0.121305(0.003\%) \\ \pi^{160}: \text{Set III} \quad a_1 &= 0.0850(14.2\%) \\ &a_2 = 0.121272(0.003\%) \end{aligned}$$

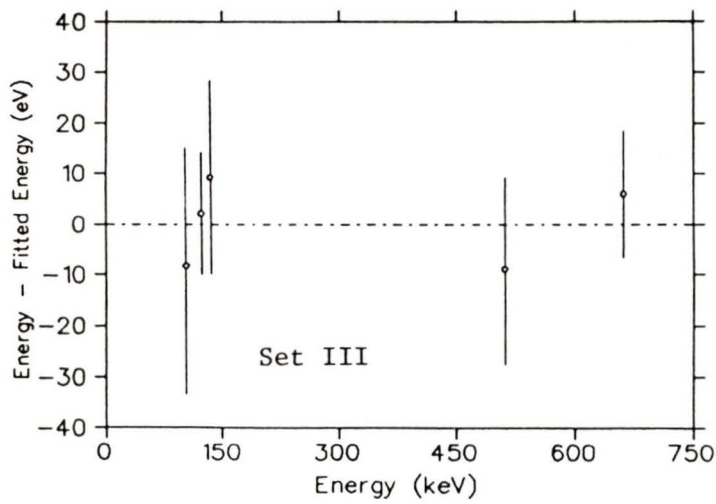
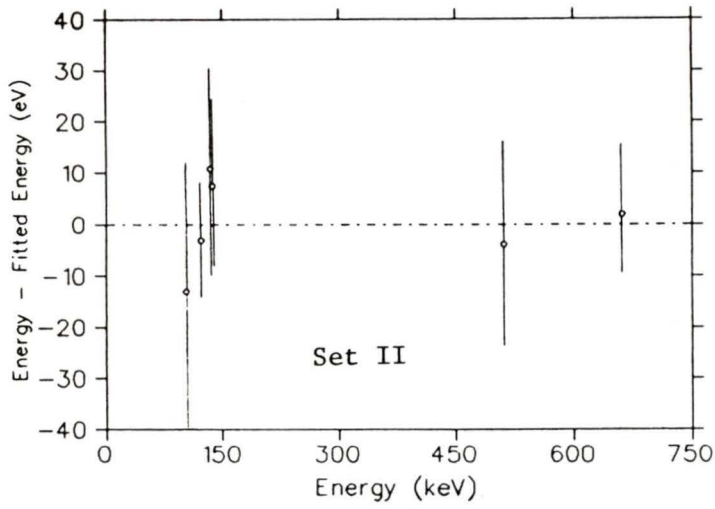
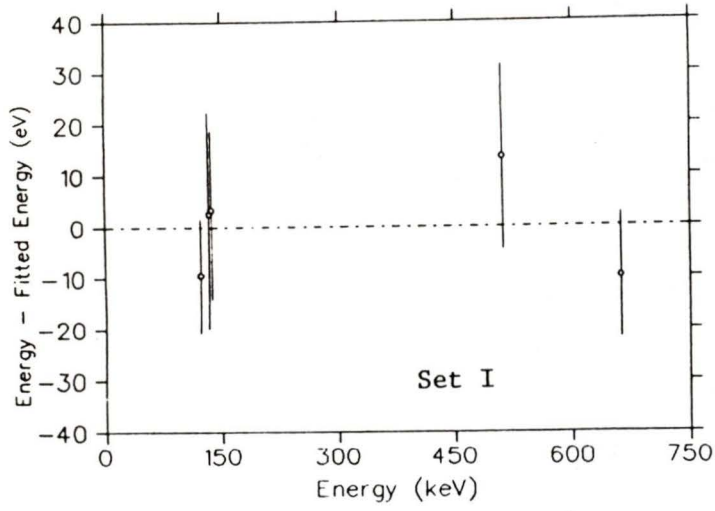


Figure 14: Energy Calibration

Analysis of the π ^{16}O 2p-1s X-ray Line

The first step in the analysis was the determination of the parameters of the detector response function in the region of the 2p-1s X ray. The resolution and tailing parameters were then fixed at those values. In the case of ^{16}O there was only one set of data to be analyzed. The detector efficiency function was also included in the fitting function used for Lorentz-broadened lines.

In the final analysis the background was fitted to a linear function although the effects of an exponential background and a step background were investigated. The effects on the energy and width of the X ray due to the choice of background type are included in the uncertainties. The effects due to a step background are included with the uncertainty due to the tailing parameters. The uncertainty attributed to background in Table 10 is estimated from the difference between linear and exponential functions.

The choice of fit region affected the determination of the background and hence the energy and width of the broadened peak. The different regions chosen are shown on Figure 15 and approximate those used in two previous analyses of the 2p-1s X ray: the narrower region was used by Sayre (1982) and the wider region by Schwanner et al. (1984).

Results quoted are based on the wider fit region and the effects due to the choice of fitting window included in the uncertainty.

The peaks in the fit regions are also shown in Figure 15 (the data points are plotted as '+' and the solid line simply joins the data points) and their fitted energies and intensities are listed in Table 6. The gamma ray line at 169 keV was due to inelastic neutron scattering in the ^{12}C present in the scintillators and the target holder plastic. No higher energy lines that could produce a Compton edge in the fit region were found in the prompt spectrum.

The intensity of the π 180 2p-1s X-ray peak in the 160 spectrum was fixed at 0.2%, the natural abundance of that isotope. The final fit to the data is shown in Figure 16, as a solid line, and the various contributions to the uncertainties are shown in Table 10.

Figure 15: $\pi^{16}\text{O}$ Regions and Peaks

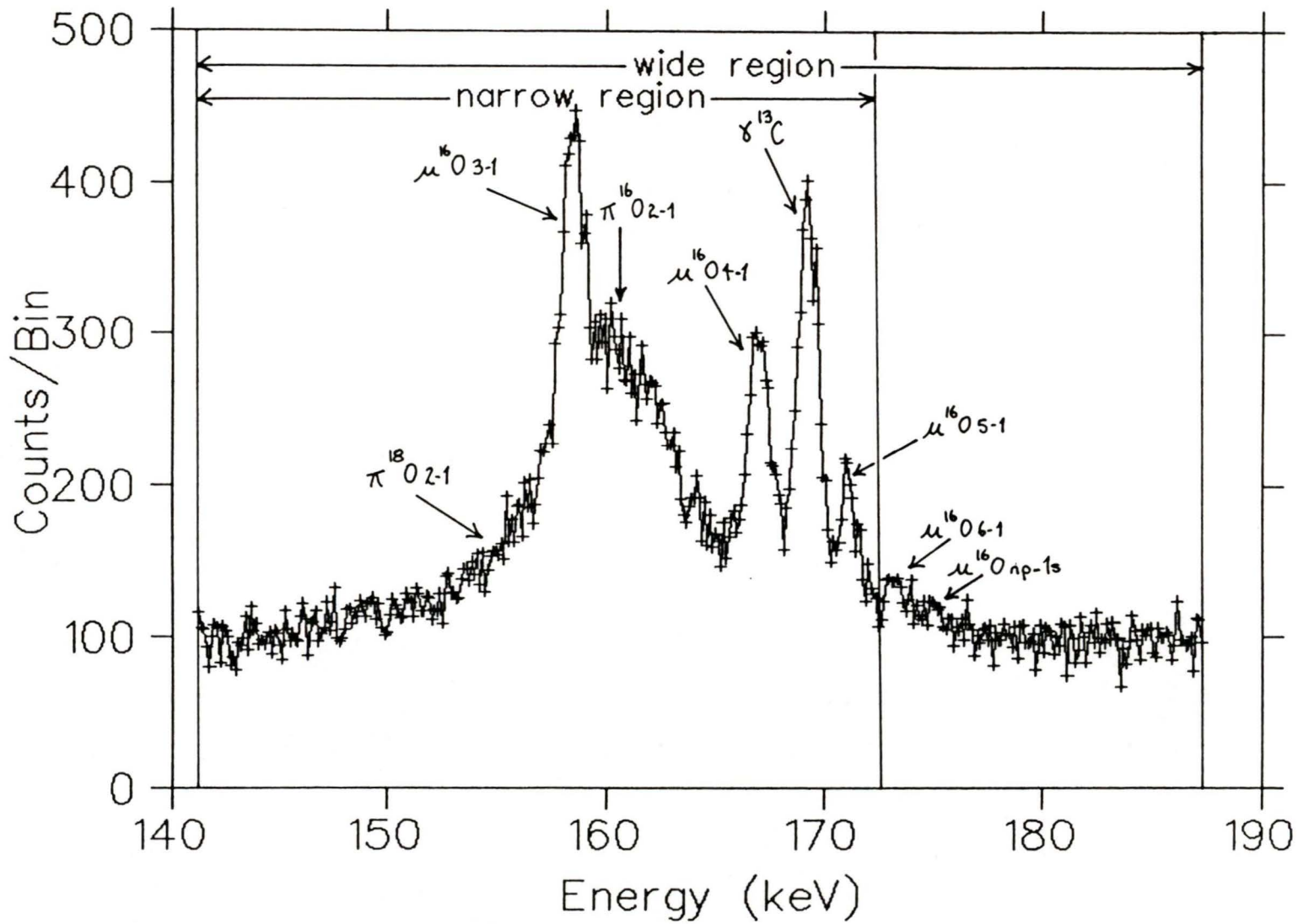


Figure 16: $\pi^{16}\text{O}$ Final Fit

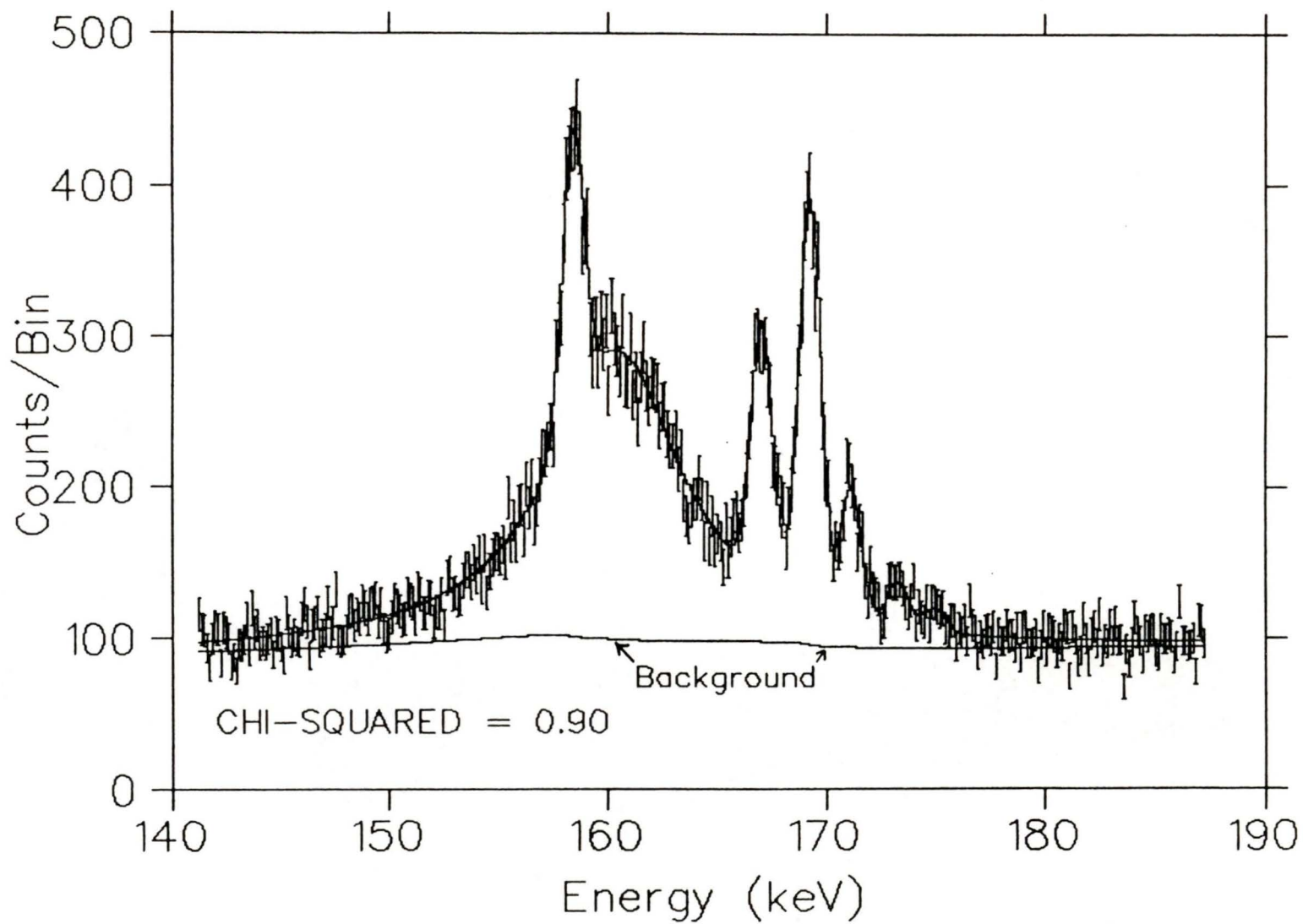


Table 6 Peaks in the $\pi^{16}\text{O}$ 2p-1s Fitting Window

Peak	Energy (keV) ¹	Intensity (events)
$\pi^{18}\text{O}$ 2p-1s	156.045 fixed	35 fixed
$\mu^{16}\text{O}$ 3p-1s	158.400 (0.028)	1931 (88)
$\pi^{16}\text{O}$ 2p-1s	160.389 (0.067)	17576 (434)
$\mu^{16}\text{O}$ 4p-1s	167.050 (0.026)	1723 (63)
$\gamma^{13}\text{C}$	169.260 (0.020)	2757 (68)
$\mu^{16}\text{O}$ 5p-1s	171.166 (0.040)	883 (50)
$\mu^{16}\text{O}$ 6p-1s	173.280 (0.050)	310 (43)
$\mu^{16}\text{O}$ np-1s	174.940 (0.174)	165 (41)

(1) The errors shown are 1σ errors.

Analysis of the π^{180} 2p-1s X-ray Line

As in the analysis of the π^{160} X ray the resolution and tailing parameters were fixed at previously determined values and the efficiency function was included in the fitting program. The background was taken to be a linear function and, as was done in the analysis of the π^{160} 2p-1s X ray, the effects of different background functions and fit regions were investigated.

A peak at 298 keV was noted in the prompt spectrum which would have produced a Compton edge at about 160 keV. However, the BGO suppression system reduced the Compton edge of the 356 keV gamma ray line in the ^{133}Ba source spectrum to a negligible size, and it was found that the Compton edge of the 298 keV peak was likewise reduced to a negligible size. The peaks in the π^{180} 2p-1s fitting windows are shown in Figure 17 and their energies and intensities are listed in Tables 7 and 8. The positions of the π^{160} 2p-1s and π^{170} 2p-1s X-ray lines were fixed and their intensities were fixed at the manufacturer's specified isotopic purity of 1.5% and 0.5%, respectively.

Figure 17: π ^{18}O Regions and Peaks

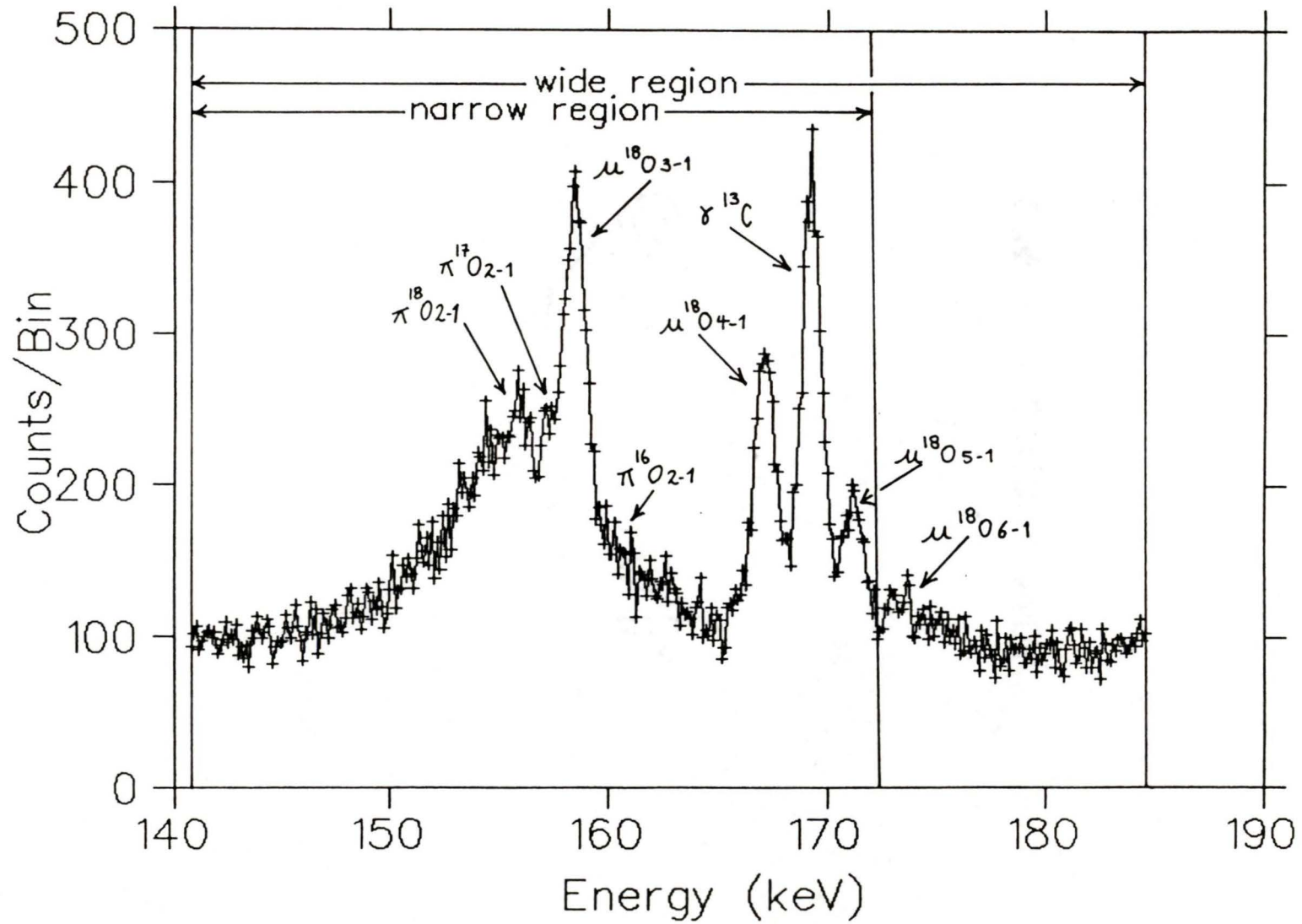


Table 7 Peaks in the π^{180} 2p-1s Fitting
Window (Set I)

Peak	Energy (keV) ¹	Intensity (events)
π^{180} 2p-1s	156.053 (0.101)	7313 (334)
π^{170} 2p-1s	158.223 fixed	40 fixed
μ^{180} 3p-1s	158.519 (0.032)	1137 (64)
π^{160} 2p-1s	160.389 fixed	118 fixed
μ^{180} 4p-1s	167.122 (0.028)	1127 (46)
$\gamma^{13}\text{C}$	169.242 (0.022)	1679 (52)
μ^{180} 5p-1s	171.096 (0.042)	640 (40)
μ^{180} 6p-1s	173.492 (0.125)	164 (32)

(1) The errors shown are 1σ errors.

Table 8 Peaks in the $\pi^{18}\text{O}$ 2p-1s Fitting
Window (Set II)

Peak	Energy (keV) ¹	Intensity (events)
$\pi^{18}\text{O}$ 2p-1s	156.034 (0.085)	13820 (497)
$\pi^{17}\text{O}$ 2p-1s	158.209 fixed	69 fixed
$\mu^{18}\text{O}$ 3p-1s	158.493 (0.026)	1925 (84)
$\pi^{16}\text{O}$ 2p-1s	160.389 fixed	213 fixed
$\mu^{18}\text{O}$ 4p-1s	167.156 (0.023)	1845 (62)
$\gamma^{13}\text{C}$	169.282 (0.018)	2959 (71)
$\mu^{18}\text{O}$ 5p-1s	171.209 (0.035)	976 (52)
$\mu^{18}\text{O}$ 6p-1s	173.380 (0.080)	350 (44)

(1) The errors shown are 1σ errors.

The percentage of ^{16}O in the ^{18}O target is known to have a significant effect on the experimentally measured energy and width of the $\pi^{18}\text{O}$ 2p-1s X ray and so the effects of the percent ^{16}O content assumed in the fits to the data were investigated further. The intensity of the $\pi^{16}\text{O}$ 2p-1s X-ray line was also determined to be $< 5\%$ in a subsequent π^- elastic scattering experiment performed on the same H_2^{18}O liquid. The effects on the energy and width of the $\pi^{18}\text{O}$ 2p-1s X ray as the percentage of ^{16}O is increased from 1.5% to 5% are included in the uncertainty. A 'free fit' of the intensity of the $\pi^{16}\text{O}$ X ray yielded a value consistent with zero in Set I of the $\pi^{18}\text{O}$ data and a value of $9\% \pm 5\%$ in Set II. As the percent ^{16}O content increased from 1.5% to 5%, both the energy and width of the $\pi^{18}\text{O}$ X ray decreased, as would be expected.

The final fits to the data are shown in Figures 18 and 19 and the various contributions to the uncertainties are shown in Table 10.

Figure 18: $\pi^{18}\text{O}$ Final Fit (Set I)

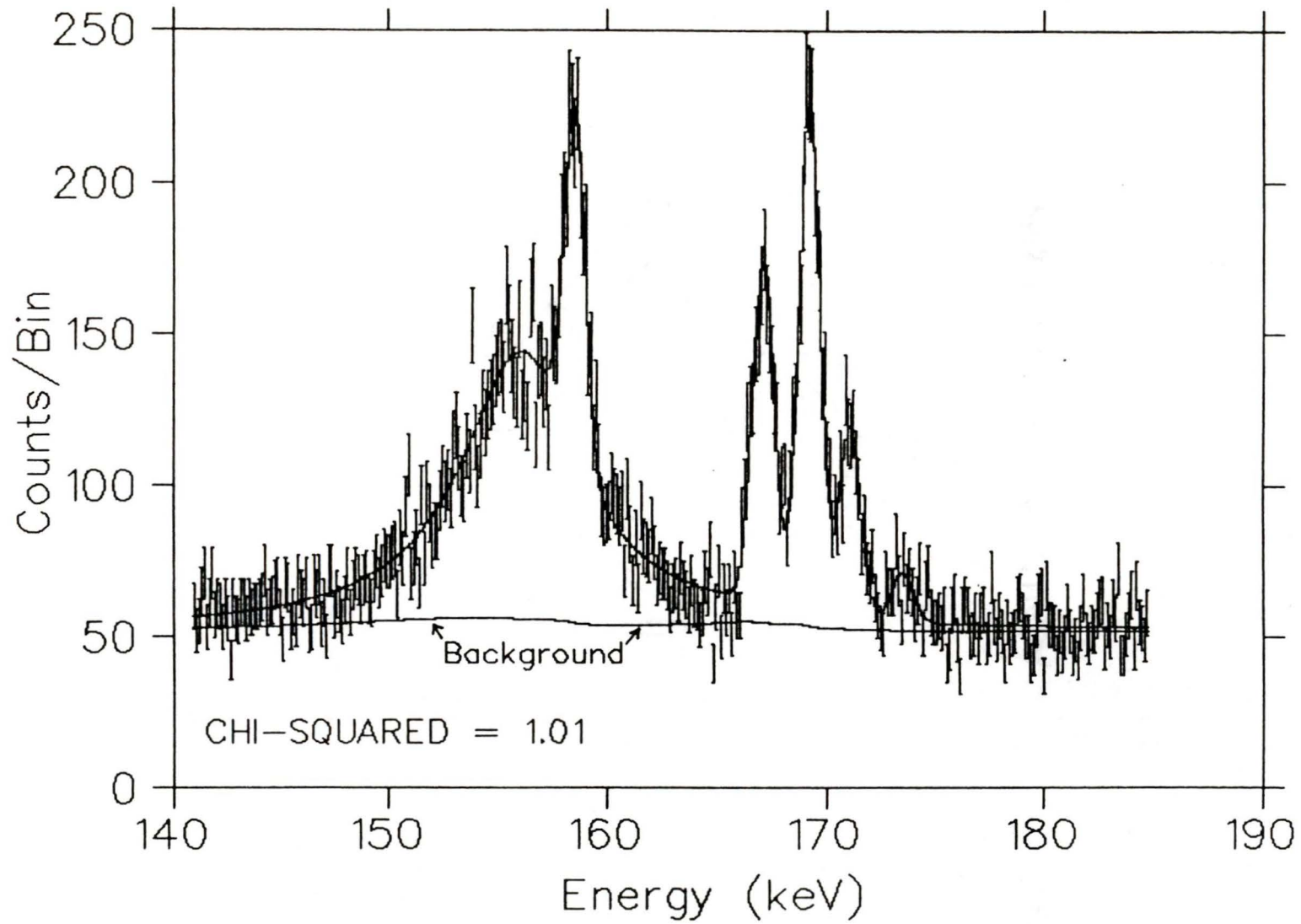


Figure 19: π ^{18}O Final Fit (Set II)

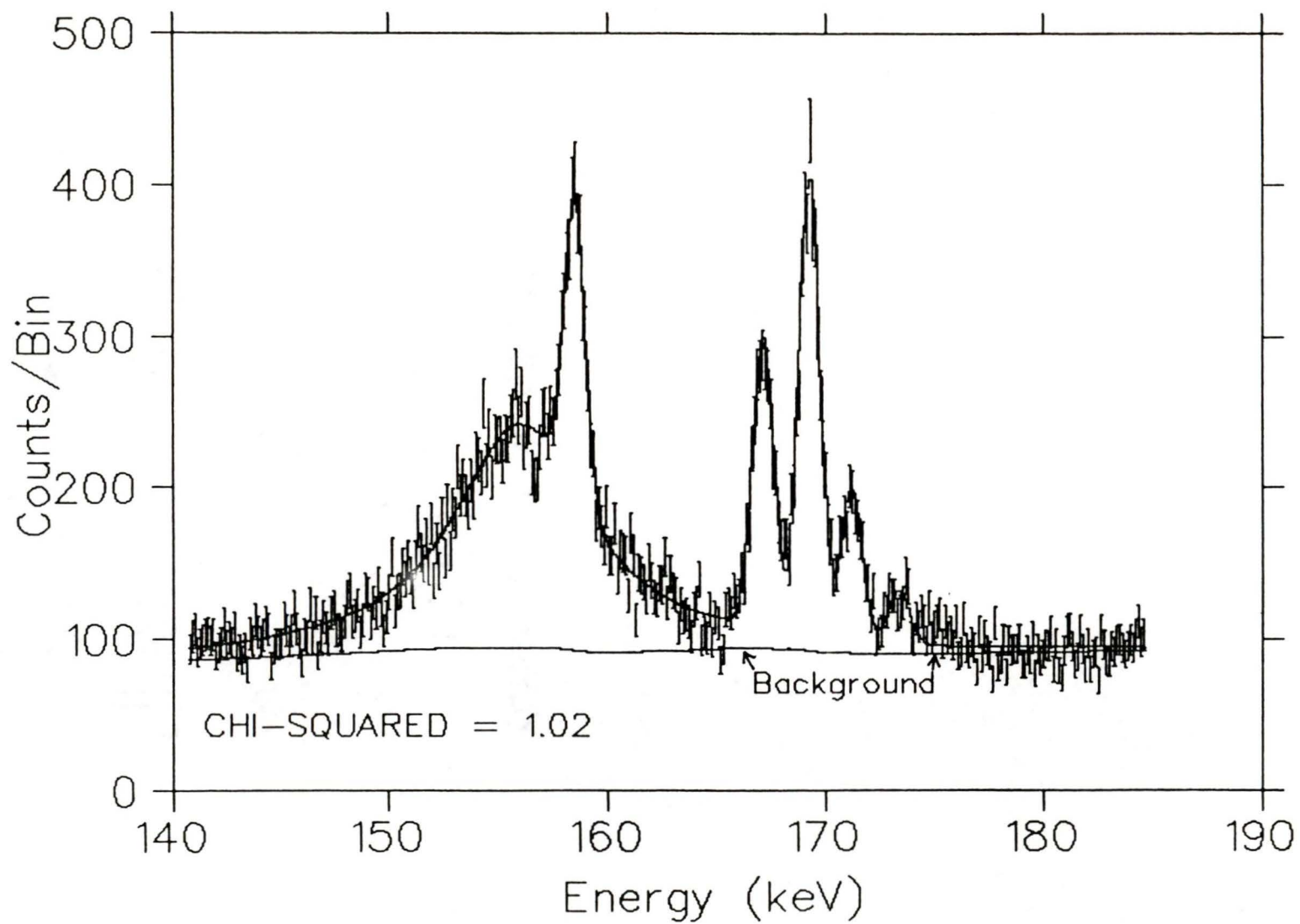


Table 9 Final Results		
	Energy (keV)	Width (keV)
^{16}O 2p-1s	160.388 (0.083)	6.94 (0.31)
^{18}O (I)	156.053 (0.145)	6.29 (0.44)
(II)	156.034 (0.139)	7.13 (0.45)
Weighted Average	156.044 (0.119)	6.71 (0.39)

Table 10 Contributions to the Uncertainties in the Energies and Widths of the π $^{16},^{18}\text{O}$ 2p-1s X rays						
	^{18}O (I)		^{18}O (II)		^{16}O (III)	
	ΔE (eV)	$\Delta\Gamma$ (eV)	ΔE (eV)	$\Delta\Gamma$ (eV)	ΔE (eV)	$\Delta\Gamma$ (eV)
Statistics	101	321	85	280	67	209
Tailing	46	190	52	200	45	189
Resolution	35	20	40	40	5	75
Efficiency	5	3	6	3	5	-
Calibration	12	-	12	-	13	-
Background	5	6	7	7	5	5
Fit Region	30	116	37	150	10	90
% ^{16}O	80	200	78	250	-	-
Totals	145	439	139	453	83	305

CHAPTER 5

DISCUSSION OF RESULTS AND CONCLUSIONSTheoretical Predictions

The optical model calculations were performed using the code of Krell and Ericson (1969) which includes the effects of finite size and vacuum polarization. The theoretical widths and shifts of the 16,180 2p-1s X rays depend on the particular optical potential function and parameters chosen. An outline of the calculation of the transition energies and level widths for the π 16,180 systems is given here, following the procedure outlined in the work by Sayre (1982).

The strong interaction potential model (II) parameters of Poffenberger (1980) were used. These parameters, obtained from a global fit to the best pionic X-ray data for light nuclei available at the time, are shown in Table 11. Data from several nuclei with non-zero isospin were included in the fit to determine the isovector terms, however the only data available for isospin 1 nuclei were from 180 . Due to the disagreement in past measurements (Schwanner et al., 1980; Sayre, 1982) of the energies of the 2p-1s transitions in 16,180 , a weighted average of the two results was used in the analysis by Poffenberger.

Table 11 Optical Potential Parameters			
$b_0 (m_\pi^{-1})$	$b_1 (m_\pi^{-1})$	$c_0 (m_\pi^{-3})$	$c_1 (m_\pi^{-3})$
-0.0155	-0.0949	0.241	0.0
$\text{Re } B_0 (m_\pi^{-4})$	$\text{Im } B_0 (m_\pi^{-4})$	$\text{Im } C_0 (m_\pi^{-6})$	ξ
-0.0501	0.04545	0.112	1.0

The energies of pionic X-ray transitions are dependent on the nuclear charge densities (or rms charge radii). Values used in obtaining the theoretical transition energies of Table 13 are shown in Table 12. The neutron radii are from π^- elastic scattering results (Johnson et al., 1979). The error shown for r_n (^{18}O) is due to the uncertainty in the isotopic purity of the target used in the scattering experiment. The charge radii are from the elastic electron scattering measurements of Miska et al. (1979). The values of r_p were obtained from the rms charge radii by unfolding the proton and neutron charge and magnetic form factors, shown in Table 12 as the Total Charge Form Factor (TCFF).

Table 12 Charge and Matter Distributions Used in the Theoretical Calculations of Energies and Linewidths				
	$\langle r^2 \rangle^{1/2}$ (fm)	r_n (fm)	r_p (fm)	TCFF ¹ (fm)
¹⁶ O	2.720	2.59	2.61	0.766
¹⁸ O	2.794	2.79 ± .03	2.70	0.718

1) From Poffenberger (1980).

The strong interaction shifts, ϵ , are defined by

$$\epsilon = E_{\text{exp}} - E_{\text{em}} \quad (39)$$

where E_{em} is the purely electromagnetic value that includes the effects of finite size and vacuum polarization and E_{exp} is the experimentally measured value. The errors in the theoretical $\pi 0 2p-1s$ energies and linewidths were due to the uncertainties in the optical model and charge distribution parameters.

Comparison of Results With Theory and Other Experiments

The results of this work are compared in Table 13 to all other published results and the theoretical calculations discussed in the previous section. Also included in Table 13 are the previous results obtained by the University of Victoria group. In Figures 20 and 21 the previous experimental results are compared.

The 160 results are in good agreement with the optical model predictions, but such is not the case with the 180 results. This may be due to the fact that the global fit used only data from one isospin 1 nucleus (an average of previous 180 data) in determining the optical model parameter b_1 . Transition energies in the non-isospin-zero nuclei are highly dependent on the difference between r_n and r_p , with the values of r_n being difficult to measure. In addition, there also exists an interdependence between the values of r_n and b_1 .

Previous experimental results, excluding those obtained by the TRIUMF group, are significantly different from the present results, except for the 180 width and the 160 width of the SIN and CERN groups, respectively. Agreement of the present results with the previous measurements carried out at TRIUMF is good.

Table 13 Comparison of the Measured Energies, Shifts and Widths of the $\pi^{16,180}$ 2p-1s X rays With Other Experiments and Theory

160			
	E (keV)	ϵ (keV)	Γ (keV)
TRIUMF (1)	160.388(.083)	-15.02(.09)	6.94(.31)
TRIUMF (2)	160.286(.090)	-15.13(.13)	7.32(.30)
SIN (3)	159.900(.090)	-15.43(.10)	7.92(.32)
CERN (4)	159.95(.25)	-15.73(.26)	7.56(.50)
Theory (5)	160.293(.15)	-15.12(.17)	7.33(.24)
180			
	E (keV)	ϵ (keV)	Γ (keV)
TRIUMF (1)	156.044(.119)	-19.38(.13)	6.71(.39)
TRIUMF (2)	155.792(.160)	-19.63(.20)	5.97(.59)
SIN (3)	155.417(.115)	-19.92(.11)	6.33(.43)
CERN (4)	155.01 (.25)	-20.59(.26)	8.67(.7)
Theory (5)	155.59 (.39)	-19.84(.41)	5.73(.46)

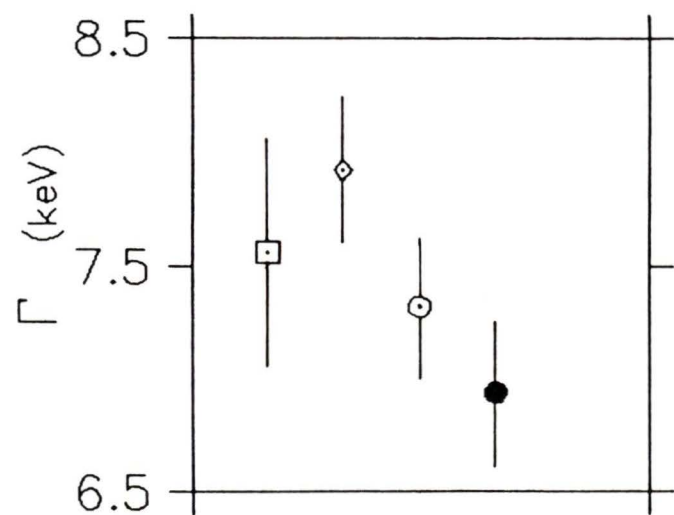
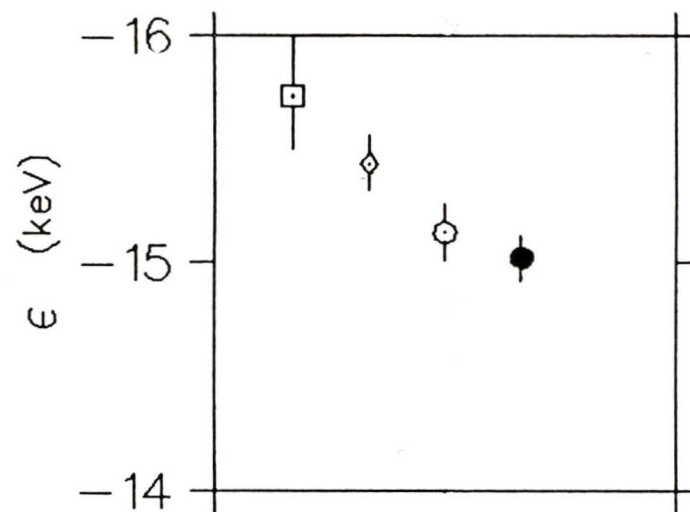
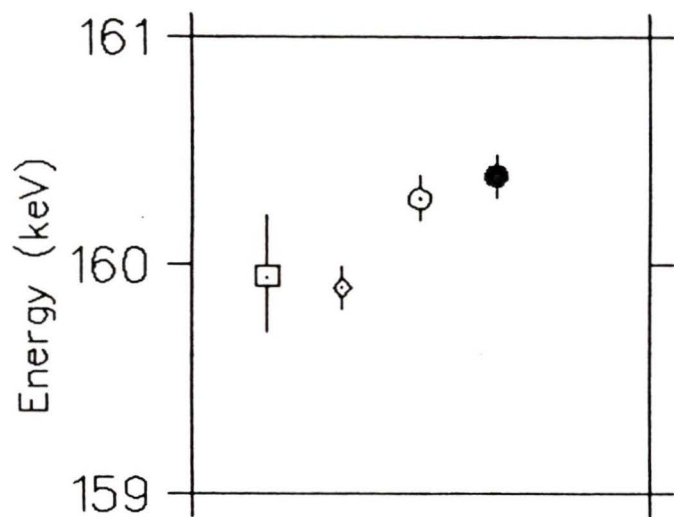
(1) Present experiment.

(2) Sayre (1980).

(3) Schwanner et al. (1984).

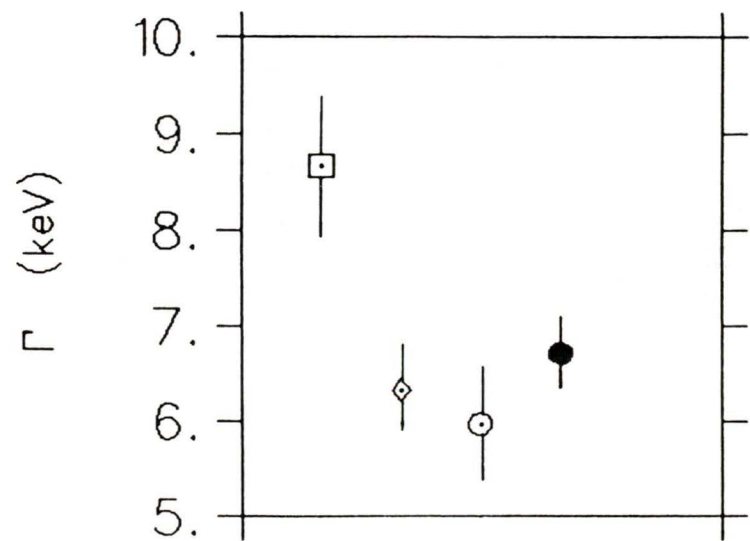
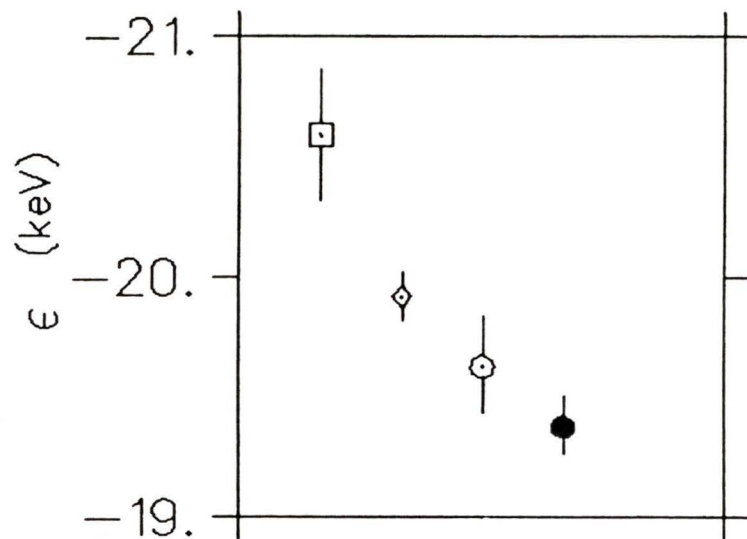
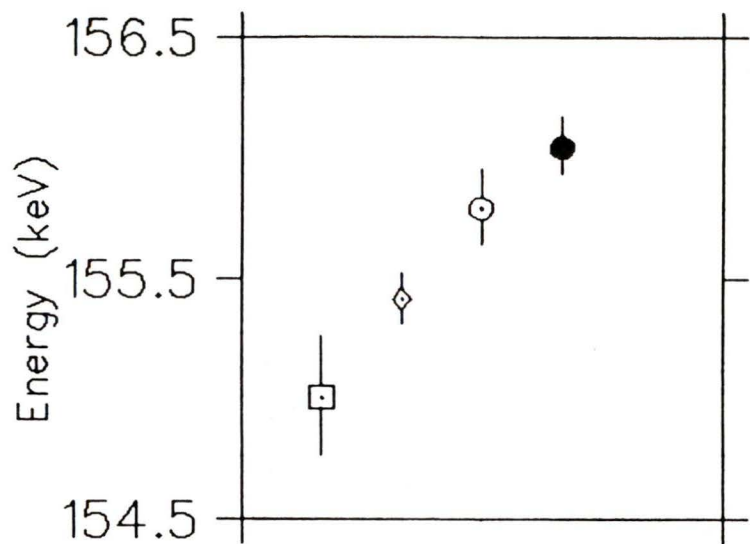
(4) Backenstoss et al. (1967).

(5) Optical model (II) of Poffenberger (1980).



- CERN
- ◇ SIN
- TRIUMF2
- TRIUMF1

Figure 20: Comparison of Experimental π ^{16}O 2p-1s Energies, Shifts and Widths



- CERN
- ◇ SIN
- TRIUMF2
- TRIUMF1

Figure 21: Comparison of Experimental π ^{18}O 2p-1s Energies, Shifts and Widths

The width of the π^{160} 2p-1s line is three standard deviations away from the SIN result. The 180 width, however, is seen to be in agreement with the two most recent measurements. In the past it was noted (Sayre, 1982) that the width of the π^{180} 2p-1s line was smaller than that of the π^{160} 2p-1s line, a reversal of the earlier CERN results. In the present analysis it was found that the difference in the widths of the two lines is now consistent with zero.

A major difference between the present experiment and those performed in the past was the use of the Compton suppression system. This gave a much improved peak-to-background ratio as compared to previous experiments. The reason for the differences in width might be found in the sensitivity of the width to the shape of the background as seen in previous analyses of the experimental data. The background in this analysis was found to be linear and effects on the width of the X ray due to an exponential background were found to be minimal. The π Cl 3d-2p X ray line, present in previous experimental spectra, played no role in the fitting of the 2p-1s X rays. The location of the Cl line (itself of Lorentzian shape), on the low energy side of the X ray, could have had an effect on the determination of the width of the X ray.

The present pionic 2p-1s X-ray energies are higher, by about five standard deviations, for both isotopes than the SIN results, but are in agreement with the previous TRIUMF results. These differences can not be due to a difference in energy calibration since the energies of the muonic transitions as determined in this experiment (shown in Table 14) can be seen to be in excellent agreement with past results, with the exception of the $\mu^{18}\text{O}$ 3p-1s transition. (The experimental energies of this transition differ by 73 eV, a much smaller difference than that between the energies of the 2p-1s X rays.) In addition, the energy of the $5/2^+ \rightarrow 3/2^-$ nuclear transition in ^{13}C was determined to be 169.266 ± 0.014 keV from the $\pi^{18}\text{O}$ data and 169.260 ± 0.020 keV from the $\pi^{16}\text{O}$ data, in agreement with previous measurements (Ajzenberg-Selove, 1976).

Systematic differences in the experimental energies of the broadened pionic X rays could arise from the use of different lineshape models in the fitting programs used by the two groups. This could lead to differences of equal sign and nearly equal magnitude in the fitted energies of broadened peaks with approximately the same shape and intensity, as in the 2p-1s X-ray lines. However, this systematic behavior is not observed in the widths, and agreement is not good in this case either.

Table 14 Comparison of Experimental Energies (in keV) of the $\mu^{16,180}$ np-1s X rays			
		160	
	(1)	(2)	(3)
2p-1s	133.516(.019)	133.536(.009)	133.525(.015)
3p-1s	158.400(.024)	158.448(.015)	158.408(.015)
4p-1s	167.050(.034)	167.081(.015)	167.114(.015)
5p-1s	171.166(.052)	171.113(.022)	171.144(.016)
		180	
	(1)	(2)	(3)
2p-1s	133.546(.020)	133.535(.009)	133.553(.016)
3p-1s	158.525(.030)	158.422(.025)	158.452(.027)
4p-1s	167.166(.029)	167.148(.047)	167.165(.032)
5p-1s	171.186(.036)	170.933(.036)	171.198(.050)

(1) Present experiment.

(2) Sayre (1982).

(3) Backenstoss et al. (1980).

The isotope effects

$$\Delta\epsilon_{1s} = \epsilon_{1s}^{(180)} - \epsilon_{1s}^{(160)}$$

$$\Delta\Gamma_{1s} = \Gamma_{1s}^{(180)} - \Gamma_{1s}^{(160)}$$

are shown in Table 15. In the case of $\Delta\epsilon$, agreement with recent results is good. However, the $\Delta\Gamma$ results are in disagreement and the possible reasons for this disagreement have been discussed previously.

Table 15 Isotope Effects Compared to Other
Experiments and Theory

	$\Delta\epsilon$ (keV)	$\Delta\Gamma$ (keV)
TRIUMF (1)	-4.36(.16)	-0.23(.50)
TRIUMF (2)	-4.50(.24)	-1.35(.66)
SIN (3)	-4.49(.14)	-1.30(.50)
CERN (4)	-4.86(.38)	1.01(.86)
Theory (5)	-4.72(.44)	-1.60(.52)

(1) Present experiment.

(2) Sayre (1982).

(3) Schwanner et al. (1984)

(4) Backenstoss et al. (1967)

(5) From optical model (II) results of Poffenberger
(1980).

Conclusions

In an attempt to resolve the disagreements between previous results, pionic oxygen measurements were repeated using a recently-constructed Compton Suppression Spectrometer. A much improved peak-to-background ratio and a better definition of contaminant lines permitted a more confident determination of the 2p-1s level widths than was previously possible.

In light of this new measurement and recent experiments by the TRIUMF group to measure pionic 2p-1s transitions in ^{22}Ne , ^{23}Na and ^{24}Mg it would be interesting to again investigate the global fit to pionic atom data for light nuclei. In particular, a more accurate measurement of the isotope effects in the $^{20,22}\text{Ne}$ isotope pair, combined with the $^{16,18}\text{O}$ data, would lead to a better determination of the values of the isovector terms in the optical potential model of the strong interaction.

REFERENCES

- F. Ajzenberg-Selove, Nucl. Phys., A268 (1976) 1.
- G. Backenstoss, S. Charalambus, H. Daniel, H. Koch,
G. Poelz, H. Schmitt, and L. Tauscher, Phys. Lett.,
25B, (1967) 365.
- G. Backenstoss, Ann. Rev. Nucl. Science, 20 (1970) 467.
- G. Backenstoss, W. Kowald, I. Schwanner, L. Tauscher,
H.J. Weyer, D. Gotta, and R. Guigas, Phys. Lett.,
95B, (1980) 212.
- K.A. Brueckner, R. Serber and K.M. Watson, Phys. Rev., 84
(1951) 258.
- M. Camac, A.D. McGuire, J.B. Platt and H.J. Schulte, Phys.
Rev., 88 (1952) 134.
- R. Engfer, H. Schneuwly, J.L. Vuilleumier, H.K. Walter, and
A. Zehnder, Atomic Data and Nuclear Data Tables, 14
(1974) 509.
- M. Ericson and T.E.O. Ericson, Ann. of Phys., 36 (1966) 323.
T.E.O. Ericson, The Pion-Nucleus Interaction,
Proceedings of the Banff Summer School on Intermediate
Energy Nuclear Physics, p. 102, Eds. G.C. Neilson,
W.C. Olsen, and S. Varma, University of Alberta,
1970.
- E. Fermi and E. Teller, Phys. Rev., 72 (1947) 399.

- E. Friedman and A. Gal, Nucl. Phys., A345 (1980) 457.
- F.S. Goulding and R.H. Pehl, Semiconductor Radiation
Detectors in Nuclear Spectroscopy and Reactions, ed.
J. Cerny, Academic Press, New York, 1974.
- F. James and M. Roos, Comp. Phys. Communications, 10, (1975)
343.
- R.R. Johnson, T. Masterson, B. Bassalleck, W. Gyles, T.
K.L. Erdman, A.W. Thomas, D.R. Gill, E. Rost, J.J.
Kraushaar, J. Alster, C. Sabev, J. Arvieux, and M.
Krell, Phys. Rev. Lett., 43 (1979) 844.
- M. Krell, The Pionic (Kaonic) Atom Program: PIATOM,
University of Victoria, TRIUMF Report VPN-77-5, 1977.
- M. Krell and T.E.O. Ericson, Nucl. Phys., B11 (1969) 521.
- C.M.G. Lattes, H. Muirhead, G.P.S. Ochialini, and C.F.
Powell, Nature, 159 (1947) 694.
- M. Lax, Rev. Mod. Phys., 23 (1952) 287.
- S.M. Li, M.Sc. Thesis, University of Victoria, 1985.
- E.L. Mathie, M.Sc. Thesis, University of Victoria, 1976.
- H. Miska, B. Norum, M.V. Hynes, W. Bertozzi, S. Kowalski,
F.N. Rad, C.P. Sargent, T. Sasanuma, and B.L. Berman,
Phys. Lett., 83B (1979) 165.
- A. Olin, "Jagspot: A Code for Fitting Complex Gamma Ray
Spectra", University of Victoria TRIUMF Report
VPN-78-2.

- A. Olin, P.R. Poffenberger, and D.I. Britton, Nucl. Instr. and Meth. 222 (1984) 463.
- P.R. Poffenberger, Ph.D. Thesis, University of Victoria (1980).
- R.J. Powers, K.C. Wang, M.V. Hoehn, E.B. Shera, H.D. Wohlfahrt and A.R. Kunselman, Nucl. Phys., A336 (1980) 475.
- C.I. Sayre, M.Sc. Thesis, University of Victoria, 1982.
- I. Schwanner, R. Abela, G. Backenstoss, W. Kowald, P. Pavlopoulos, L. Tauscher, H.J. Weyer, P. Blum, M. Dorr, W. Fetscher, D. Gotta, R. Guigas, H. Koch, H. Poth, G. Schmidt, and H. Ullrich, Phys. Lett. 96B (1980) 268.
- I. Schwanner, G. Backenstoss, D. Gotta, W. Kowald, L. Tauscher, H. Ullrich, and H.J. Weyer, Nucl. Phys., A412 (1984) 253.
- E. Storm and H.I. Israel, Photon Cross-Sections, Nuclear Data Tables A, 7 (1970) 565.
- J.A. Wheeler, Phys. Rev., 71 (1947) 320.
- W.S.C. Williams, An Introduction to Elementary Particles, Academic Press, New York, 1971.
- H. Yukawa, Proc. Phys. Math. Soc. of Japan, 17 (1935) 48.

VITA

Surname: ROUTENBURG Given Names: PAUL ARTHUR

Place of Birth: Markdale, Ontario

Date of Birth: November 23, 1960

Educational Institutions Attended, with Dates of Entering
and Leaving:

University of Waterloo, Waterloo, Ont. 1978 to 1983

University of Victoria, Victoria, B.C. 1983 to 1985

Degrees, Diplomas, Etc., Awarded, with Dates and Names of
Institutions:

B.Sc. (Honours) 1983 University of Waterloo

PARTIAL COPYRIGHT LICENSE

I hereby grant the right to lend my thesis or dissertation (the title of which is shown below) to users of the University of Victoria Library, and to make single copies only for such users or in response to a similar request from the Library of any other university or similar institution, on its behalf or for one of its users. I further agree that permission for extensive copying of this thesis for scholarly purposes may be granted by me or by a member of the University designated by me. It is understood that copying or publication of this thesis for financial gain shall not be allowed without my written permission.

Title of Thesis:

Pionic 2p-1s Transitions in ^{16,18}O

Author:



PAUL ROUTENBURG

August, 1985.